Lithos 354–355 (2020) 105346

Contents lists available at ScienceDirect

Lithos

journal homepage: www.elsevier.com/locate/lithos

Research article

Reworking of old continental lithosphere: Unradiogenic Os and decoupled Hf—Nd isotopes in sub-arc mantle pyroxenites

Romain Tilhac [a,*], Beñat Oliveira [a], William L. Griffin [a], Suzanne Y. O'Reilly [a], Bruce F. Schaefer [a], Olivier Alard [a,b], Georges Ceuleneer [c], Juan Carlos Afonso [a,d], Michel Grégoire [a,c]

[a] ARC Centre of Excellence for Core to Crust Fluid Systems (CCFS) and GEMOC, Department of Earth and Planetary Sciences, Macquarie University, Sydney, NSW 2109, Australia
[b] Géosciences Montpellier, UMR 5243, CNRS, Université Montpellier, 34095 Montpellier, France
[c] Géosciences Environnement Toulouse (GET), Université de Toulouse, CNRS, IRD, 14 avenue E. Belin, 31400 Toulouse, France
[d] Centre for Earth Evolution and Dynamics, University of Oslo, Norway

ARTICLE INFO

Article history:
Received 18 March 2019
Received in revised form 13 December 2019
Accepted 16 December 2019
Available online 21 December 2019

Keywords:
Radiogenic isotopes
Isotopic decoupling
Highly siderophile elements (HSE)
Melt-peridotite interaction
Amphibolitization
Arc-continent interaction

ABSTRACT

Mantle lithologies in orogenic massifs and xenoliths commonly display strikingly different Hf- and Nd-isotope compositions compared to oceanic basalts. While the presence of pyroxenites has long been suggested in the source region of mantle-derived magmas, very few studies have reported their combined Hf—Nd isotope compositions. We here report the first Lu—Hf data along with Re—Os data and S concentrations on the Cabo Ortegal Complex, where the pyroxenite-rich Herbeira massif has been interpreted as remnants of a delaminated arc root. The pyroxenites, chromitites and their host harzburgites show a wide range of whole-rock $^{187}Re/^{188}Os$ and $^{187}Os/^{188}Os$ (0.16–1.44), indicating that Re was strongly mobilized, partly during hydrous retrograde metamorphism but mostly during supergene alteration that preferentially affected low-Mg#, low Cu/S pyroxenites. Samples that escaped this disturbance yield an isochron age of 838 ± 42 Ma, interpreted as the formation of Cabo Ortegal pyroxenites. Corresponding values of initial $^{187}Os/^{188}Os$ (0.111–0.117) are relatively unradiogenic, suggesting limited contributions of slab-derived Os to primitive arc melts such as those parental to these pyroxenites. This interpretation is consistent with radiogenic Os in arc lavas being mostly related to crustal assimilation. Paleoproterozoic to Archean Os model ages confirm that Cabo Ortegal pyroxenites record incipient volcanic arc magmatism on the continental margin of the Western African Craton, as notably documented by zircon U—Pb ages of 2.1 and 2.7 Ga. Lu—Hf data collected on clinopyroxene and amphibole separates and whole-rock samples are characterized by uncorrelated $^{176}Lu/^{177}Hf$ and $^{176}Hf/^{177}Hf$ (0.2822–0.2855), decoupled from Nd-isotope compositions. This decoupling is ascribed to diffusional disequilibrium during melt-peridotite interaction, in good agreement with the results of percolation-diffusion models simulating the interaction of an arc melt with an ancient melt-depleted residue. These models notably show that Hf—Nd isotopic decoupling such as recorded by Cabo Ortegal pyroxenites and peridotites ($\Delta\varepsilon_{Hf(i)}$ up to +97) is enhanced during melt-peridotite interaction by slow diffusional re-equilibration and can be relatively insensitive to chromatographic fractionation. Finally, we discuss the hypothesis that arc-continent interaction may provide preferential conditions for such isotopic decoupling and propose that its ubiquitous recognition in peridotites reflects the recycling of sub-arc mantle domains derived from ancient, reworked SCLM.

1. Introduction

Application of the Lu—Hf isotope systematics to oceanic lavas has significantly contributed to understanding the evolution of the Earth's crust-mantle system (*e.g.* Blichert-Toft and Albarède, 1997). On the one hand, $^{143}Nd/^{144}Nd$ and $^{176}Hf/^{177}Hf$ in mid-ocean ridge (MORB) and ocean-island basalts (OIB) define a linear Hf—Nd mantle array (Patchett and Tatsumoto, 1980), probably reflecting the contribution of recycled oceanic basalts and sediments to the depleted mantle (Chauvel et al., 2008). On the other hand, abyssal peridotites commonly have highly radiogenic Hf- and Nd-isotope compositions (*e.g.* Byerly and Lassiter, 2014) suggesting the existence of ultra-depleted domains in the convective mantle (Salters et al., 2011). In contrast, peridotite xenoliths and orogenic massifs have radiogenic Hf compositions decoupled from Nd isotopes and plotting well above the Hf—Nd mantle array (*e.g.* Bizimis et al., 2003; Pearson and Nowell, 2004; Salters and Zindler, 1995). To account for this decoupling, models of melt-peridotite interaction involving ancient and/or variously depleted mantle domains (Bizimis et al., 2003; Sanfilippo et al., 2019; Stracke et al.,

* Corresponding author.
E-mail address: romain.tilhac@mq.edu.au (R. Tilhac).

https://doi.org/10.1016/j.lithos.2019.105346
0024-4937/

2011) have been formulated on the basis of the relative mobility of Nd with respect to Hf (*e.g.* Bedini et al., 2004), among others (Ionov et al., 2005; Schmidberger et al., 2002).

In the lithospheric mantle, melt-peridotite interaction has been proposed to explain the origin of many pyroxenites (*e.g.* Garrido and Bodinier, 1999; Montanini and Tribuzio, 2015). Pyroxenites are a volumetrically minor component in the upper mantle, yet they are often invoked in models of basalt petrogenesis (Lambart et al., 2016, and references therein). The presence of pyroxene-rich lithologies in the mantle may result from recycling of oceanic crust, melt segregation and melt-peridotite interaction, and lithospheric delamination (Tilhac et al., 2016, and references therein). All these mechanisms are all likely to occur in the mantle wedge and sub-arc lithospheric mantle (*e.g.* Kelemen et al., 2014) and pyroxenites are accordingly abundant in xenoliths derived from the sub-arc mantle (Sorbadere et al., 2013, and references therein). Importantly, pyroxenites are associated with melt-peridotite interaction at low and/or decreasing melt mass, with potentially important consequences for parent-daughter fractionation in isotopic systems of different geochemical affinities. However, relatively few studies have reported combined Hf- and Nd-isotope compositions of pyroxenites (Ackerman et al., 2016; Bizimis et al., 2005; Lu et al., 2018; Montanini et al., 2012; Pearson and Nowell, 2004) and even fewer have included spinel pyroxenites (Pearson and Nowell, 2004).

In the Cabo Ortegal Complex, high-pressure mineral segregation and melt-peridotite interaction in a sub-arc mantle have been documented in the pyroxenite-rich Herbeira massif (Tilhac et al., 2016). The pyroxenites and their host peridotites also record deformational and metamorphic overprints associated with subduction, possibly following delamination of the arc root (Henry et al., 2017; Santos et al., 2002; Tilhac et al., 2016). This provides a rare opportunity to investigate how the formation and recycling of pyroxenites may contribute to the isotopic variability of the upper mantle. We have therefore applied Lu—Hf isotope systematics to a set of well-characterized pyroxenites and peridotites and the results are compared with numerical percolation-diffusion models. In addition, Os-isotope compositions have been measured in the pyroxenites, peridotites and associated chromitites. Re and Os are chalcophile elements in the mantle and thus offer a complementary perspective to the one provided by incompatible lithophile elements. Os isotopes also benefit from large parent-daughter fractionation during mantle melting thanks to the extremely compatible nature of Os (Carlson, 2005, and references therein). As such, they have been invaluable in the identification of ancient mantle signatures and subduction-related metasomatism (*e.g.* Parkinson et al., 1998; Widom, 2011). By examining the Os-isotope compositions of otherwise poorly documented sub-arc mantle lithologies, we also intend to contribute to understanding the origin of relatively radiogenic Os measured in many arc lavas (Alves et al., 2002).

2. Geodynamic and geological background

2.1. Peri-Gondwanan arc magmatism and the origin of Cabo Ortegal pyroxenites

Cambro-Ordovician arc magmatism on the northern Gondwanan margin is documented in north-western Iberia by the presence of voluminous volcanic series and sedimentary sequences and by detrital zircons derived from the West African Craton (Albert et al., 2015; Roper, 2016), among others. Allochthonous metamorphic complexes now preserve remnants of these arcs and ophiolites (Fig. 1a), along with the partially subducted Gondwanan margin and a serpentinized mélange (*e.g.* Albert et al., 2015; Arenas et al., 2009), forming a rootless suture assembled during the Variscan orogeny (Martínez Catalán et al., 2009). In the Cabo Ortegal Complex, Galicia (north-western Spain), ultramafic rocks are associated in a high-pressure (HP), high-temperature (HT) unit with granulites, eclogites and gneisses (Fig. 1b). The latter are heterogeneous paragneisses whose contacts are outlined by ultramafic rocks interpreted as mantle fragments incorporated into the subduction zone (Gil Ibarguchi et al., 1999). The eclogites have been interpreted as a metamorphosed volcano-sedimentary sequence (Albert et al., 2012) while the granulite protoliths are uncertain, potentially including volcanic-arc upper crust (Galán and Marcos, 1998). The ultramafic rocks are exposed in three main massifs; the largest, Herbeira (~12.5 km^2), is the object of this study (Fig. 1c). It consists of a harzburgite-dominated domain with minor pyroxenites (<10%), dunites and chromitites, and of a heterogeneous domain successively exposing (1) dunites and chromitites (Fig. 2a), (2) pyroxenites interlayered with dunites (Fig. 2b) or harzburgites, and locally chromitites (Fig. 2c) and (3) harzburgites (Fig. 2d). Individual pyroxenite layers can exceed 100 m in length and reach up to 3 m in thickness (Girardeau et al., 1989). They also can be thinly foliated and highly amphibolitized, locally as hornblendites.

Based on petrological and geochemical data summarized in the next section, Tilhac (2017) proposed a petrogenetic scenario (Fig. 3) corresponding to the intrusion of a Si-undersatured (picritic) melt in a sub-arc lithospheric mantle. This episode, thereafter referred to as the main magmatic episode, led to the formation of dunites and chromitites as products of melt interaction with the host harzburgites, and of olivine-bearing clinopyroxenites partially replacing the dunites (preserved as lenses) as melt differentiation occurred along the clinopyroxene-olivine cotectic line. Olivine-free websterites and subordinate orthopyroxene-rich websterites were either formed *via* a peritectic reaction during the process above (Fig. 3a) or crystallized as dykes from initially Si-rich (boninitic) melts (Fig. 3b). Late-magmatic amphibole crystallized upon cooling from hydrous residual melts responsible for the metasomatic enrichment of the pyroxenites and peridotites. The age of this episode is poorly constrained by Rb—Sr and Sm—Nd ages between 459 and 515 Ma reported for pyroxenites and peridotites (Santos et al., 2002; Tilhac et al., 2017, and references therein), overlapping zircon U—Pb ages of the eclogite and granulite protoliths (Ordóñez Casado et al., 2001).

2.2. Deformational and metamorphic overprint during subduction and collision

The compositional layering of peridotites and pyroxenites resulting from the main magmatic episode is parallel to a HT (>1000 °C) foliation (Henry et al., 2017). The related deformation episode (D_{HT}) was responsible for isoclinal folding and boudinage of the pyroxenite layers (Girardeau and Gil Ibarguchi, 1991). It is overprinted by a HP deformation episode (D_1) common to all HP-HT units, characterized by elongated sheath folds and mylonites along tectonic contacts (Ábalos et al., 2003, and references therein) and ascribed to subduction channel processes (Puelles et al., 2012). The latter clearly post-dates the pyroxenites formation (Tilhac et al., 2016), suggesting that D_1 may have followed arc root delamination as a result of the negative buoyancy of pyroxenites with respect to refractory peridotites (Müntener et al., 2001), in good agreement with prograde metamorphism which peaked under eclogite-facies conditions (1.6–1.8 GPa and 800 °C) in the ultramafic massifs (Girardeau and Gil Ibarguchi, 1991; Tilhac et al., 2016). Peak metamorphism was accompanied by the injection of mafic melts that crystallized as pyroxenite and garnet-rich dykes (clearly distinct from the main pyroxenites described above), cross-cutting the HT foliation. These dykes are dated at 383–394 Ma by U—Pb and Sm—Nd ages, coeval with the U—Pb and Rb—Sr ages (387–395 Ma) obtained from a pegmatitic granite that intruded the Uzal peridotite and with U—Pb ages (382–395 Ma) from adjacent HP-HT units (Ordóñez Casado et al., 2001, and references therein). We thus consider 390 Ma a robust age for peak metamorphic conditions in the HP-HT units of the Cabo Ortegal Complex, and this has been accordingly used for age correction in previous isotopic studies (Santos et al., 2002; Tilhac et al., 2017).

Rapid exhumation of the HP-HT units occurred *via* subduction-conduit processes by *ca* 375 Ma (Ábalos et al., 2003; Albert et al.,

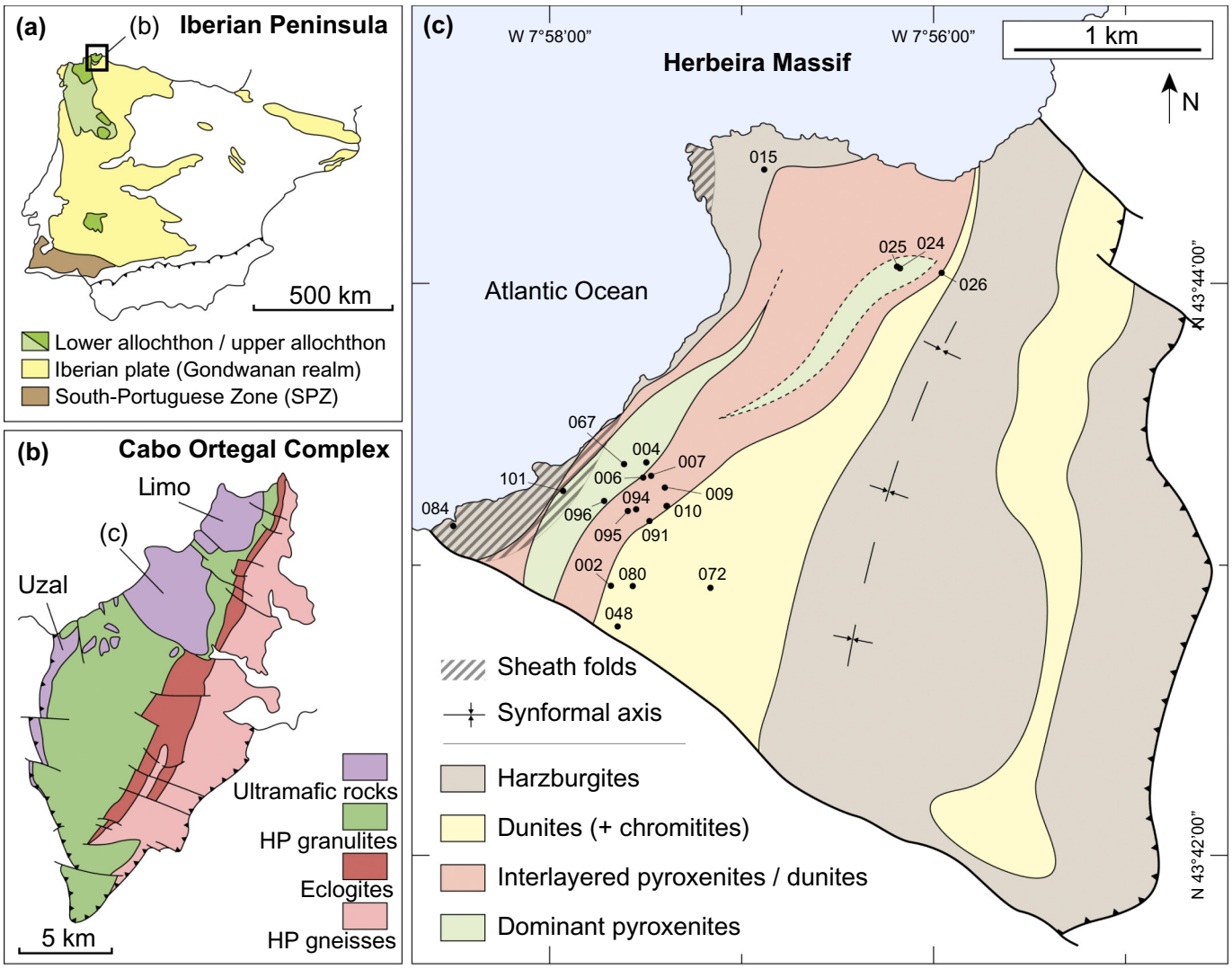

Fig. 1. (a) Location of the Cabo Ortegal Complex among the Allochthonous terranes of the Iberian Peninsula; (b) the main HP-HT units in the Upper Allochthon of the Complex (b) simplified geological map of the Herbeira massif showing sample locations used in this study (after Tilhac et al., 2016; and references therein).

2012). This episode (D_2) has been mostly reconstructed from regional cross-correlations and is only recorded in ultramafic massifs by folded D_1 structures. Exhumation continued under amphibolite- and greenschist-facies conditions, accompanied by deformation episodes D_3 and D_4, which are not documented in the ultramafic massifs apart from upright folds (Ábalos et al., 2003), such as the one responsible for the main structure of the Herbeira massif (Fig. 1c). Despite the limited deformational overprint associated with the exhumation stages, the abundance and unequivocal textural relationships of amphibole indicate some extent of metamorphic amphibolitization in the ultramafic massifs (Henry et al., 2017; Tilhac et al., 2016; Tilhac et al., 2017), in addition to the late-magmatic amphibolitization discussed above. Strong amphibolitization is particularly observed in sheath-folded areas, suggesting that the most deformed products of D_{HT} and D_1 were subsequently exposed to greater hydration, and hence amphibolitization (Tilhac et al., 2016)

3. Sample description

This study includes 18 pyroxenites (and 1 sample collected from a garnet-rich mafic layer), 2 harzburgites and 5 chromitites, all collected from the Herbeira massif of the Cabo Ortegal Complex (Fig. 1c). Major- and trace-element compositions for these samples have been reported by Tilhac et al. (2016), Sr- and Nd-isotope compositions by Tilhac et al. (2017) and petrofabric data by Henry et al. (2017).

3.1. Pyroxenites

Cabo Ortegal pyroxenites have markedly higher SiO_2, CaO, Cr and Sc contents and lower Al_2O_3, TiO_2 and Ni contents (Santos et al., 2002) than pyroxenites from most ultramafic massifs (*e.g.* Horoman, Ronda, Beni Boussera, Lanzo, Lherz). These characteristics, and their particularly high CaO/Al_2O_3 and large ion lithophile (LILE)/high field strength elements (HFSE) are ascribed to the picritic to boninitic affinities of their parental melts (Tilhac et al., 2016). They exhibit enriched mantle I (EMI)-like Sr-isotope compositions ($^{87}Sr/^{86}Sr = 0.7037–0.7048$) and a negative correlation between Nd isotopes (ε_{Nd} between 2 and −8) and light rare earth element (LREE) enrichment (Tilhac et al., 2017). The samples used in this study are representative of the four types of pyroxenite identified by Tilhac et al. (2016), including a composite sample (CO-010). Type-1 pyroxenites are olivine-bearing clinopyroxenites and websterites preserving dunite lenses; they have high Mg# (87–89) and Cr_2O_3 (0.63–0.84 wt%), low Al_2O_3 (1.8–3.4 wt%) and TiO_2 (<0.09 wt%) and spoon-shaped REE patterns [most $(La/Gd)_{CN} < 1$; CN indicates chondrite-normalized]. Type-2 pyroxenites are massive websterites

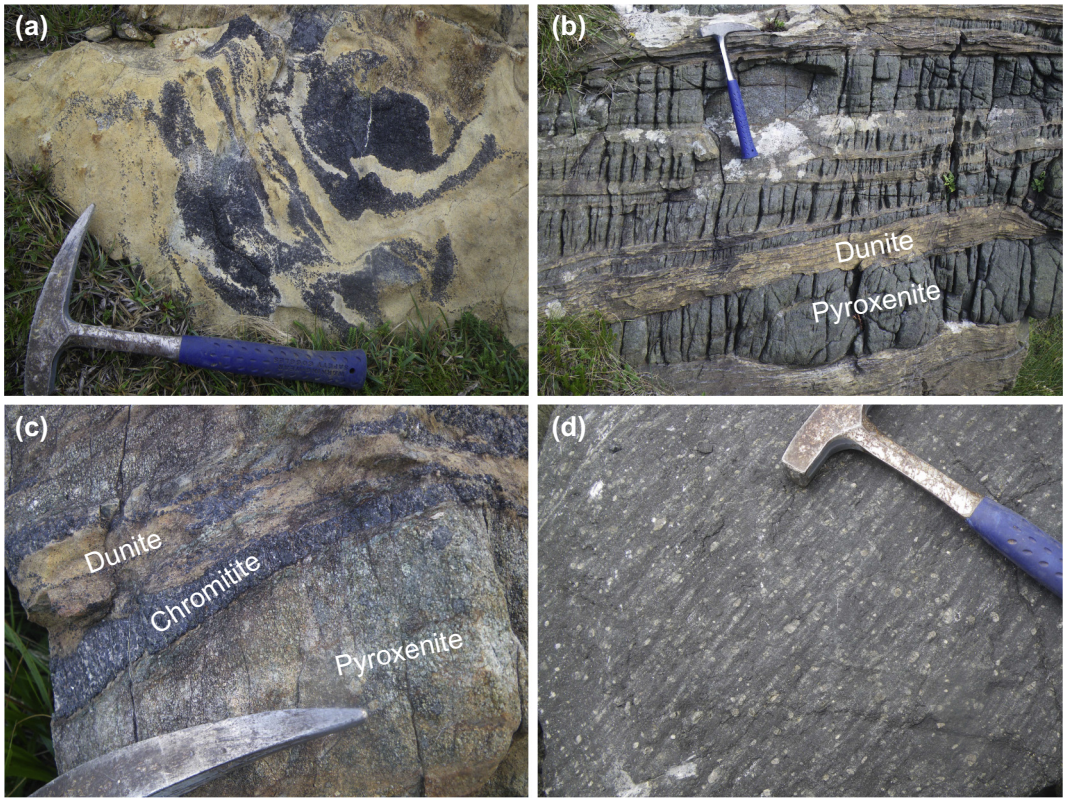

Fig. 2. Field photographs illustrating typical exposures (from top to bottom of the Herbeira cliffs) of dunites and chromitites (a), pyroxenites interlayered with dunites (b), and locally chromitites (c), and the host harzburgite (d).

and clinopyroxenites with higher Al_2O_3 (2.8–5.9 wt%), and lower Mg# (83–87); they exhibit a wide range of LREE enrichment [$(La/Gd)_{CN}$ = 1.1–3.2]. Type-3 pyroxenites are thinly foliated clinopyroxenites, and to a minor extent websterites, commonly highly amphibolitized and with a range of Mg# (84–90) overlapping that of type-1 and -2 pyroxenites; they have slightly higher K_2O (0.04–0.27 wt%) and Na_2O (0.08–0.78 wt%) contents and strong LREE enrichment [$(La/Gd)_{CN}$ = 2.6–8.6]. Type-4 pyroxenites are volumetrically subordinate

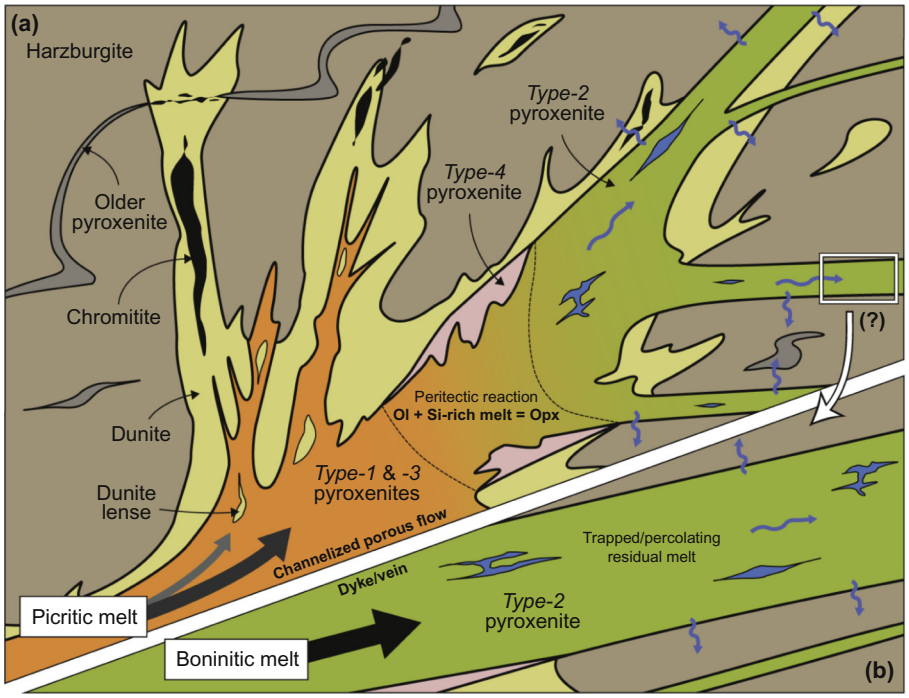

Fig. 3. Schematic representation of the model proposed by Tilhac (2017) for the main magmatic episode in the petrogenesis of Cabo Ortegal pyroxenites, dunites and chromitites, assuming an initially picritic (a) and/or boninitic (b) melt. Subsequent reactions during prograde and retrograde metamorphic episodes are omitted (see text for further detail). Note the extremely deformed (older) pyroxenites (not included in this study) that are dissolved at the contact with dunites leaving disseminated chromites behind.

orthopyroxene-rich websterites and orthopyroxenites with high Mg# and Cr#.

In all types of pyroxenite, clinopyroxene (clinopyroxene) is well preserved, either as exsolved porphyroclasts or exsolution-free granoblasts and/or neoblasts. Orthopyroxene (orthopyroxene) occur as relatively fresh neoblasts but mostly as deformed and variously serpentinized porphyroclasts with clinopyroxene and spinel exsolution needles. Olivine is restricted to type-1 pyroxenites as lenses, interstitial trails between pyroxenes and inclusions in pyroxenes; it is generally fresher than dunitic olivine not hosted in pyroxenites. Spinel occurs either as discrete inclusions, exsolved needles and vermicular grains in silicates, or as large interstitial grains locally associated with sulfides. Garnet is restricted to a few type-2 pyroxenites where it occurs in different textural assemblages, either in equilibrium with pyroxenes or as coronas around spinel formed by prograde metamorphism (*e.g.* CO-024). It is also found in garnet-rich areas forming bands in pyroxenite or veins in mylonitic harzburgite, where it encloses pyroxenes in a poikilitic texture (CO-006-B) and in the garnet-rich layer (CO-026) described by Girardeau and Gil Ibarguchi (1991). Amphibole occurs in proportions varying between types from 5 to 42 wt% (Table 1), either clearly post-kinematic, replacing clinopyroxene (±spinel) and preferentially grown among matrix minerals, or as pre- to *syn*-kinematic xenomorphic grains in textural equilibrium with clinopyroxene. Fine-grained sub-idiomorphic to idiomorphic amphibole occurs within pyroxenes, located associated with spinel along clinopyroxene cleavages and replacing clinopyroxene exsolution lamellae in orthopyroxene. At high degrees of amphibolitization (mainly in type 3 pyroxenites and rare hornblendites), amphibole growth has resulted in sutured grain boundaries and composite porphyroclastic and/or poikilitic textures (Tilhac, 2017). Henry et al. (2017) confirmed these observations with electron back-scattered diffraction (EBSD) data showing that xenomorphic grains are more internally deformed that idiomorphic grains and estimated that ~20% of the amphibole by volume was probably pre-kinematic, while the rest relates to metamorphic overprinting.

Base-metal sulfides (BMS) occur up to ~1% in volume as well-preserved (<20% of alteration products such as Fe oxyhydrodrides) interstitial grains formed of pyrrhotite, pentlandite and blocky chalcopyrite, locally associated with spinel (Fig. 4a) and/or amphibole (Fig. 4b). They show curvilinear boundaries (Fig. 4a) and low dihedral angle and are commonly elongated (aspect ratio >1:2 to 1:4), particularly where necked by silicates (Fig. 4b). Although these interstitial sulfides are particularly large (*i.e.* from several hundreds of μm to >1 mm), their occurrence is characteristic of pyroxenite occurrences elsewhere (*e.g.* Lorand, 1991). Their mineralogy and microstructural relationships with silicates suggest that they probably represent exsolved products after primary sulfides crystallized (± amphibole) from an intercumulus melt. BMS less commonly occur as small (50–100 μm) rounded inclusions in silicates, internally more homogeneous than interstitial grains with particularly less chalcopyrite and more pyrrhotite. Rare platinum-group minerals (PGM), mainly Pt-Pd-rich tellurides, bismuthides and arsenides occur as thin needles in sulfides.

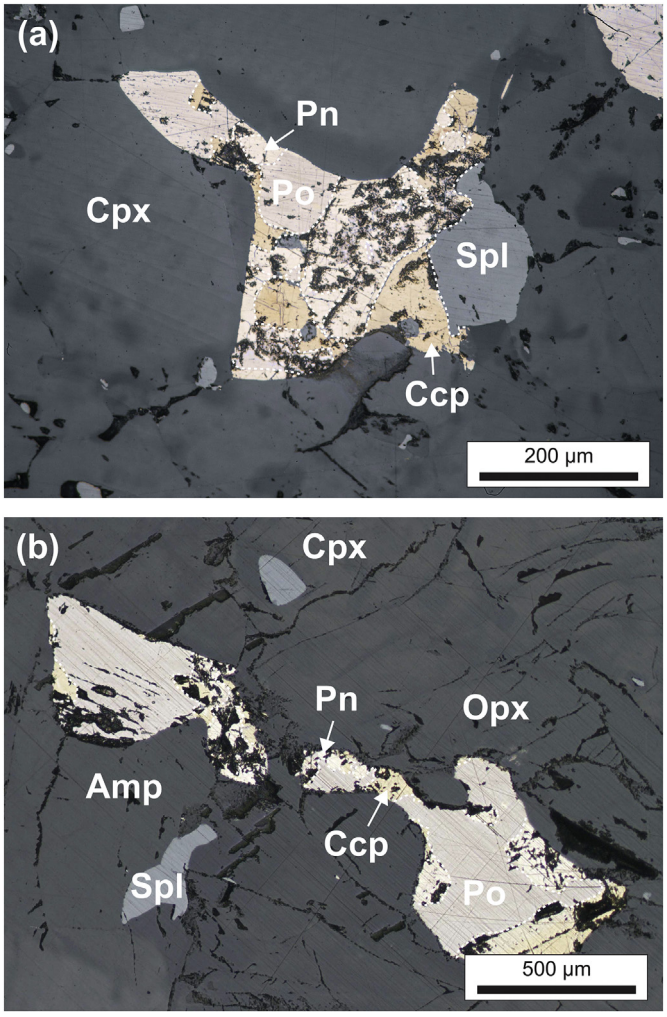

Fig. 4. Photomicrographs of representative interstitial base-metal sulfides in Cabo Ortegal pyroxenites. Note the low dihedral angle and association with spinel (a) and amphibole (b). Pn, pentlandite; Po, pyrrhotite; Ccp, chalcopyrite.

Table 1
S abundances, Cu/S and $(La/Sm)_{CN}$ ratios and amphibole contents.

Sample	S (ppm)	Cu/S	Ampibole (wt%)	$(La/Sm)_{CN}$
Type-1 pyroxenites				
CO-094-B	n.a.	n.a.	8.0	0.82
CO-095-A	736	0.25	6.7	3.93
CO-096-B	1276	0.22	8.3	1.09
Type-2 pyroxenites				
CO-006-A	531	0.18	26.0	0.003
CO-007	164.6	1.4	10.9	3.35
CO-024	530	0.08	17.9	1.72
CO-025	1190	0.10	18.9	1.44
Type-3 pyroxenites				
CO-004-A	80.6	0.92	42.5	3.74
CO-010-1	294	1.4	11.8	4.21
CO-010-2	652	0.42	8.6	5.68
CO-010-3	655	0.46	7.0	9.4
CO-101	970	0.16	38.1	1.97
Type-4 pyroxenites				
CO-002-A	241	b.d.l.	5.0	n.a.
CO-048	535	0.20	5.9	4.89
Harzburgites				
CO-015-B	676	b.d.l.	5.3	64
CO-084	559	0.03	7.8	1.34
Garnet-bearing mafic layer				
CO-026	292	0.17	n.a.	2.43

Cu/S and $(La/Sm)_N$ were calculated using whole-rock Cu, La and Sm concentrations analysed by solution ICP-MS (Tilhac et al., 2016). b.d.l denotes Cu below detection limit. Modal abundance of amphibole was estimated from point counting and converted to wt% using mineral densities (Tilhac et al., 2016). n.a. not analysed.

3.2. Peridotites and chromitites

Harzburgites are variably serpentinized and amphibolitized, preserving few relics of olivine and large bastitized orthopyroxene porphyroclasts potentially derived from the disaggregation of earlier generations of pyroxenites (Fig. 3a) and rare clinopyroxene. Spinel is disseminated as fractured grains or forms elongated and discontinuous aggregates. Amphibole occurs as post-kinematic idiomorphic crystals or as exsolution lamellae in clinopyroxene. Compared to their pyroxenitic occurrence, BMS are less abundant and more altered (>50% of Fe

oxyhydroxides and magnetite) than in peridotites. They occur either as small (~50 μm) subhedral grains within the serpentine matrix, rarely enclosed in relic olivine and orthopyroxene, or as larger convoluted grains with low dihedral angles, locally associated with clinopyroxene and spinel. These sulfides are dominated by pentlandite ± chalcopyrite (±bornite along the rims) and do not exhibit the blocky texture observed in the pyroxenites. Their habitus, mineralogy and alteration features are reminiscent of sulfides in abyssal peridotites (Alard et al., 2005). A comprehensive petrological description of the peridotites is provided by Girardeau and Gil Ibarguchi (1991) and Santos et al. (2002). Among the two samples of harzburgites, CO-084 (Mg# = 88) is the freshest and has spoon-shaped LREE patterns [$(La/Sm)_{CN} = 1.3$], and CO-015-B (Mg# = 90) is more serpentinized, has more sulfides and is strongly LREE-enriched [$(La/Sm)_{CN} = 64$].

Chromitites have massive (CO-002-B, C and 072-C) and/or nodular (CO-080-B and 095-C) textures, with a serpentine (± antigorite) matrix, rarely including sub-idiomorphic chromite. In massive-textured samples, coarse grains are outlined by trails of serpentine probably replacing olivine inclusions (*e.g.* CO-072-C). Nodular chromitite occurs next to massive chromitite bands and schlieren of nodular chromites, locally associated with clinopyroxenite, wehrlite and dunite. Small BMS (~10–20 μm) are common, either as pentlandite, pyrrhotite and chalcopyrite within chromite rims, or in the serpentine matrix. They locally host PGM as individual grains or complex aggregates, commonly of Pt—Pd bearing arsenides, tellurides, sulfides, alloys and oxides. Chromitites and PGM are described in detail by Moreno et al. (2001), and references therein. Among the chromitites included in this study, samples hosted in dunite (CO-002-B, C and 080-B) are relatively Cr-rich while those associated with pyroxenites (CO-072-C and 095-C) are Al-rich (Tilhac, 2017).

4. Analytical methods

Lu—Hf isotope analyses were performed on clinopyroxene and amphibole separates and whole-rock samples of pyroxenite and peridotite, as for Sr and Nd (Tilhac et al., 2017). Clean mineral separates were hand-picked from two fractions (100–600 μm and >600 μm) obtained by sample disaggregation in a Selfrag® apparatus. Clinopyroxene and amphibole were optically pure apart from small amounts of spinel inclusions that could not be avoided. An additional aliquot of coarse-grained amphibole deliberately including abundant spinel inclusions was tested for CO-009. Splits of mineral separates were also prepared after leaching in 6 N HCl for 2 h at 80 °C, although the sample disaggregation had produced grains with visually fresh surfaces. Whole-rock samples were prepared from homogeneous slabs of sample, cleared of patina, crushed and powdered in an agate mill. The composite sample (CO-010) was cut into three slabs prepared and analysed as individual whole-rock samples. Mineral separates and whole-rock samples were digested and processed using ion-exchange techniques and up to three chromatographic columns per sample depending on the Hf concentration (Electronic Appendix 1). Hf-isotope ratios were measured by multi-collection inductively coupled plasma mass spectrometry (MC-ICP-MS) on a Nu Plasma instrument in the Geochemical Analysis Unit of GEMOC/CCFS at Macquarie University, Australia. Measurements were made in static-collection mode in Faraday cups; potential interference of ^{176}Yb on ^{176}Hf was corrected by measuring the interference-free ^{172}Yb, assuming $^{176}Yb/^{172}Yb = 0.5865$ to calculate $^{176}Yb/^{177}Hf$, then normalized to $^{179}Hf/^{177}Hf = 0.7325$ to correct for mass fractionation. Repeated analyses of Hf standard solution JMC-475 gave an average of $^{176}Hf/^{177}Hf = 0.282155 \pm 14$ (2σ; $n = 37$), within the uncertainty of the GeoRem recommended value (0.282159 ± 26; http://georem.mpch-mainz.gwdg.de). References materials BCR-2 and BHVO-2 prepared in the same way as the samples yielded $^{176}Hf/^{177}Hf = 0.282836 \pm 49$ (2σ; n = 3) and $^{176}Hf/^{177}Hf = 0.283100 \pm 11$ (2σ; $n = 9$), respectively, in good agreement with values from Jweda et al. (2016) for BCR-2 (0.282866 ± 11), and the GeoRem recommended value for BHVO-2 (0.283109 ± 12), respectively. Blanks were generally below 60 pg. $^{176}Lu/^{177}Hf$ ratios were calculated from their relative isotopic abundances and elemental ratios measured by high-precision laser ablation (LA)-ICP-MS data for mineral separates, and solution ICP-MS for whole-rock samples (Tilhac et al., 2016). LA-ICP-MS analyses of reference materials yielded 0.50 ± 0.02 ppm Lu and 5.02 ± 0.18 ppm Hf for BCR-2 (2σ; $n = 31$), and 0.28 ± 0.04 ppm Lu and 4.43 ± 0.27 ppm Hf for BHVO-2 (2σ; $n = 146$). Solution ICP-MS analyses of reference material PM-S yielded 0.15 ± 0.03 ppm Lu and 1.07 ± 0.02 ppm Hf. These concentrations are in good agreement with the GeoRem recommended values.

Whole-rock Re—Os isotope analyses were performed on the same powders analysed for Sr, Nd and Hf. Samples were spiked with ^{190}Os and ^{185}Re for isotope-dilution measurements and digested in reverse aqua regia (RAR) in sealed Carius tubes (Electronic Appendix 2). Re and Os were separated by solvent extraction and micro-distillation and Os-isotope ratios were measured by negative-ion thermal ionization mass spectrometry (N-TIMS) on a Thermo Finnigan Triton system at Macquarie University. All analyses were carried out using a secondary electron multiplier *via* ion counting in peak hopping mode. Two replicates of reference material WPR-1 were prepared in the same way as the samples and included as unknowns in the two batches of analyses, yielding 14.93 ± 0.11 ppb Os and $^{187}Os/^{188}Os = 0.14436 \pm 5$ (2σ in-run errors) and 15.11 ± 0.02 ppb Os and $^{187}Os/^{188}Os = 0.14415 \pm 6$, respectively. These results are consistent with our long-term lab average $^{187}Os/^{188}Os = 0.14466 \pm 80$ (2σ; $n = 28$), which is in turn in good agreement with Day et al. (2016) ($^{187}Os/^{188}Os = 0.1449 \pm 13$). Os total procedural blank (TPB) levels of 1–3 pg represent contributions <0.5%, except in 4 samples with Os concentrations <140 ppt, where blank contributions rise to 1–3%. $^{187}Os/^{188}Os$ measured in the TPB was 0.1590 and 0.1642. $^{187}Re/^{188}Os$ was calculated using Re concentrations measured by isotope dilution on an Agilent 7700 ICP-MS. In-run mass bias was corrected assuming $^{187}Re/^{185}Re = 1.6739$, as measured on 1 ppb solutions run as unknown every 6th sample. The two WPR-1 yielded 9.72 ± 0.15 ppb and 10.1 ± 0.15 ppb Re (in-run errors), in good agreement with the compositions reported by Day et al. (2016). Re TPB were 12.5 and 15.0 pg for the two different batches, which represent contributions <0.1%.

A subset of whole-rock samples was analysed for their S contents using an Elementar vario EL cube elemental analyzer at Macquarie University. For each sample, ~300 mg of powder were packed in Sn-foils and ignited in an oxygen-He gas atmosphere furnace at around 1150 °C, following Huong et al. (2018). The produced gases were trapped in a set of adsorption columns. S was released upon heating at a temperature *ca* 230 °C and measured using a thermal conductivity detector. Calibration was achieved using different aliquots of sulphanilamide compound ($H_2NC_6H_4SO_2NH_2$) and reference materials BHVO2, SY4, PM-S and BAM—U110. Reference materials JP-1 and BE-N were repeatedly measured under the same analytical conditions yielding average values of 27 ± 8 and 301 ± 32 ppm (2σ; n = 3), respectively, well within error of the GeoRem recommended values.

5. Results

5.1. S concentrations

Measured S concentrations are given in Table 1. They range from 81 to 1276 ppm in pyroxenites with a marked clustering around ~600 ppm, corresponding to the concentrations obtained in the peridotites (559 and 676 ppm). No correlation between the different types of pyroxenites was observed. Duplicates (or triplicates) were analysed for 6 representative samples yielding relative external errors mostly below 15% (reaching ~30% for two samples), which is comparable with the analytical uncertainties obtained from reference materials (*i.e.* ~10% reproducibility for BE-N).

5.2. Re—Os isotope geochemistry and geochronology

Os concentrations in pyroxenites are low (0.05–0.86 ppb) while they reach 3.2–3.9 ppb in harzburgites and 25–77 ppb in chromitites (Table 2). Re concentrations are very variable, ranging from 0.36 ppb to 137 ppb in pyroxenites (Fig. 5), with one extremely high outlier (Re > 7 ppm); in the absence of duplicates due to sample unavailability, the latter value will not be discussed. The two samples of harzburgite have 1.1–4.7 ppb Re while chromitites range between 7 and 480 ppb. $^{187}Os/^{188}Os$ range between 0.16 and 0.54 in pyroxenites (one sample reaches 1.4) while peridotites and chromitites have relatively homogeneous compositions (0.132–0.138). On a log-scaled $^{187}Os/^{188}Os$ *vs* $^{187}Re/^{188}Os$ diagram (Fig. 6), these compositions are increasingly scattered from homogeneously low $^{187}Os/^{188}Os$ at low $^{187}Re/^{188}Os$ to highly heterogeneous at high $^{187}Re/^{188}Os$. However, $^{187}Re/^{188}Os$ and $^{187}Os/^{188}Os$ are well correlated in the composite, progressively LREE-enriched sample (CO-010; see Fig. 8a), defining a potential isochron age of 801 Ma (initial $^{187}Os/^{188}Os = 0.111$), or 673 Ma if the intermediate value is excluded. In good agreement with the lithophile isotopic systems Lu—Hf (this study) and Sm—Nd (Tilhac et al., 2017), the least enriched sections (2 and 3) have the least radiogenic Os ($^{187}Os/^{188}Os = 0.17–0.21$), while section 1 exhibits a higher value (0.27). Os model ages (τ_{MA}) range between 0.06 and 825 Ma (Table 2); they are mostly younger than ~60 Ma, corresponding to samples with high $^{187}Re/^{188}Os$ which give $\gamma_{Os(t)} < 0$, and suggesting recent changes in $^{187}Re/^{188}Os$. In contrast, pyroxenites with lower $^{187}Re/^{188}Os$ ratios give supra-chondritic age-corrected Os and τ_{MA} of 597–951 Ma. One harzburgite sample has sub-chondritic present-day $^{187}Os/^{188}Os$ corresponding to a Re-depletion model age (τ_{RD}) of 588 Ma.

5.3. Lu—Hf isotope geochemistry and geochronology

Hf concentrations are relatively low in Cabo Ortegal pyroxenites and peridotites (mostly <0.2 ppm). $^{176}Hf/^{177}Hf$ range between 0.2822 and 0.2855 (Table 3), with no clear correlation to $^{176}Lu/^{177}Hf$. There is no systematic distinction between the different types of pyroxenite (Fig. 7), although type-1 pyroxenites are mostly restricted to high $^{176}Lu/^{177}Hf$ because of their low Hf concentrations (*i.e.* < 0.07 ppm in clinopyroxene; Electronic Appendix 4 Fig. 1). A few type-2 pyroxenites

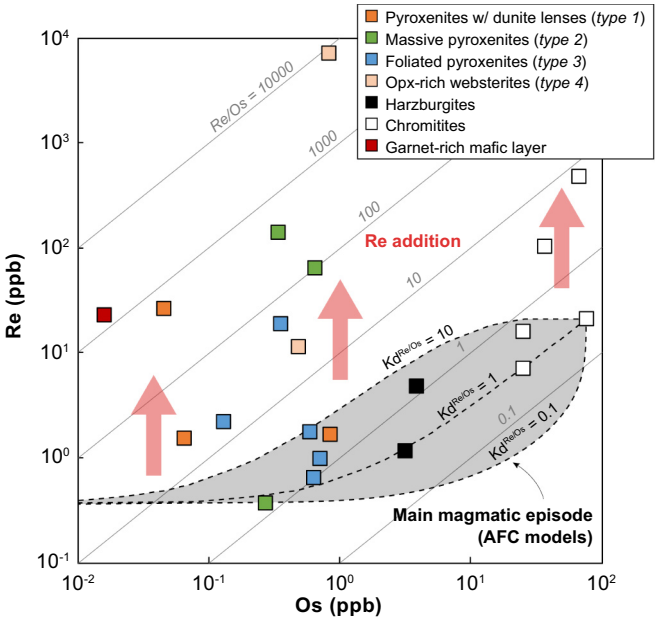

Fig. 5. Re *vs* Os concentrations in Cabo Ortegal pyroxenites, peridotites and chromitites compared with AFC models simulating the assimilation of an Os-rich end-member by an average arc melt (Alves et al., 2002). Samples with higher Re probably experienced significant post-magmatic Re addition (see text for further detail). assuming Os immobility during the Re addition (see Fig. 4 and Fig. 9a and Electronic Appendix 3 Fig. 2).

Table 2
Re and Os abundances and Os isotopic ratios of Cabo Ortegal pyroxenites, peridotites and chromitites.

Sample	Re (ppb)	Os (ppb)	$^{187}Re/^{188}Os$	$^{187}Os/^{188}Os$	2σ	γ_{Os}	$\gamma_{Os(t)}$ at 390 Ma	τ_{MA} (Ma)	τ_{RD} (Ma)
Type-1 pyroxenites									
CO-094-B	1.51	0.065	117	0.54253	21	325	−278	213	
CO-095-A	26.2	0.046	3230	1.4420	23	1030	−15,800	24	
CO-096-B	1.68	0.857	9.55	0.23620	5	85	39	708	
Type-2 pyroxenites									
CO-006-A	137*	0.341	1960	0.21984	7	72	−10,160	2.8	
CO-007	0.363	0.271	6.52	0.22530	4	77	46	951	
CO-024	63.1	0.650	469	0.15823	10	24	−2420	3.9	
CO-025		0.086		0.50054	12	292			
Type-3 pyroxenites									
CO-004-A	2.17	0.131	81.0	0.24594	18	93	−325	88	
CO-010-1	1.75	0.603	14.3	0.27823	3	118	48	648	
CO-010-2	0.971	0.710	6.7	0.21431	4	68	37	825	
CO-010-3	0.643	0.635	4.9	0.17268	4	35	13	597	
CO-101	18.8	0.360	256	0.28008	15	120	−1210	36	
Type-4 pyroxenites									
CO-002-A	11.2	0.493	111	0.22926	4	80	−494	55	
CO-048	7060*	0.827	41,300	0.16708	11	31	−215,400	0.06	
Harzburgites									
CO-015-B	4.73	3.89	5.86	0.12439	2	−2.5	−31.0		588
CO-084	1.14	3.21	1.71	0.12948	2	1.5	−5.3	87	
Chromitites									
CO-072-C	15.7	25.3	3.00	0.13818	3	8.3	−5.1	244	
CO-002-B	480	67.0	34.5	0.13519	3	6.0	−172	13	
CO-002-C	101	37.2	13.1	0.13506	3	5.9	−60	35	
CO-080-B	21.2	76.8	1.33	0.13440	3	5.4	0.6	440	
CO-095-C	6.98	25.1	1.34	0.13189	2	3.4	−1.5	275	
Garnet-bearing mafic layer									
CO-026	22.6	0.016	13,000	7.0851	463	5450	−62,000	32	

τ_{MA} and τ_{RD}, Os model age and *Re*-depletion age, respectively. Errors are given for the last digit on $^{187}Os/^{188}Os$. A decay constant of $\lambda_{Re} = 1.666 \times 10^{-11}.a^{-1}$ was used for model age calculations. γ_{Os} was calculated as $[(^{187}Os/^{188}Os_{sample})/(^{187}Os/^{188}Os_{CHUR}) - 1] \times 100$ with present-day CHUR ratios taken as $^{187}Re/^{188}Os = 0.3972$ and $^{187}Os/^{188}Os = 0.12752$ (Walker and Morgan, 1989). * denotes high uncertainties on the Re concentrations.

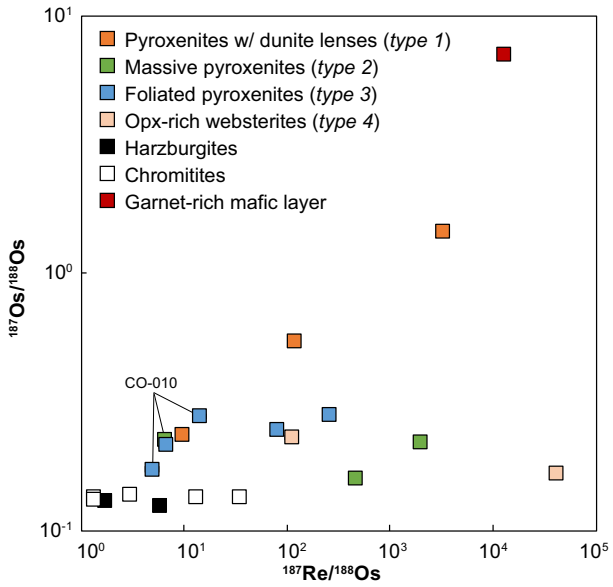

Fig. 6. Whole-rock $^{187}Os/^{188}Os$ *vs* $^{187}Re/^{188}Os$ of Cabo Ortegal pyroxenites, peridotites and chromitites showing the samples that were affected by post-magmatic Re addition. Error bars corresponding to in-run errors (2σ) are smaller than the data points. Both axes are in log scale.

also have relatively low $^{176}Hf/^{177}Hf$, while type-3 pyroxenites reach the most radiogenic values. Type-4 pyroxenites and the LREE-enriched harzburgite plot among type-1 pyroxenites while the LREE-depleted harzburgite (CO-084) exhibits more radiogenic Hf. Most whole-rock samples have slightly higher $^{176}Lu/^{177}Hf$ than corresponding clinopyroxene and their $^{176}Hf/^{177}Hf$ are within error, or at most 3×10^{-4}. Amphibole also has higher $^{176}Lu/^{177}Hf$ than coexisting clinopyroxene, but either equivalent or lower $^{176}Hf/^{177}Hf$. The coarse amphibole aliquot prepared for sample CO-004-A yields more radiogenic $^{176}Hf/^{177}Hf$ (0.2836) than its fine-grained replicate (0.2829), contrasting with Sr and Nd isotopes, for which coarse- and fine-grained amphibole were identical within error (Tilhac et al., 2017). Leached mineral separates have $^{176}Hf/^{177}Hf$ within error, or at most 5×10^{-4}, of their non-leached replicates. This result indicates the reliability of the data acquired on non-leached minerals, considering the range of variation observed between samples. There is an exception (CO-009) for which non-leached clinopyroxene and amphibole are significantly more radiogenic, indicating the presence in this particular case of a surface contaminant with radiogenic Hf and unradiogenic Sr (Tilhac et al., 2017). Among the three sections of the composite sample (CO-010; Fig. 8), as for Nd (Tilhac et al., 2017), the most LREE-enriched ones (1 and 2) have the least radiogenic Hf ($^{176}Hf/^{177}Hf$ = 0.2834–0.2840) while the least enriched one (3) yields the highest value (~0.287) measured in Cabo Ortegal pyroxenites (Fig. 7). These compositions define a Lu—Hf errorchron age of 1091 Ma, or 1052 Ma if the intermediate section is excluded (Fig. 8a), most likely representing mixing lines. Depleted-mantle model ages (τ_{DM}) reported in Table 3 range from future to unrealistically old ages; they are mostly insignificant due to the ingrowth of Hf and changes in $^{176}Lu/^{177}Hf$ as discussed in the next section.

On a present-day ε_{Hf} *vs* ε_{Nd} diagram (Fig. 9a), most type-1 pyroxenites and part of the type-2 pyroxenites (corresponding to the LREE-depleted samples; Table 3) plot near the Hf—Nd mantle array, mostly within or near the MORB-OIB field. Type-3 pyroxenites and the LREE-enriched samples of type-2 pyroxenites have a wider range of radiogenic Hf-isotope compositions, mostly plotting above ($\Delta\varepsilon_{Hf}$ up to 140) but also below the mantle array. To correct for radiogenic ingrowth over time, Hf- and Nd-isotope compositions have been calculated at the metamorphic age t = 390 Ma (Santos et al., 2002; Tilhac et al., 2017). In the resulting $\varepsilon_{Hf(t)}$ *vs* $\varepsilon_{Nd(t)}$ space (Fig. 9b), the sample distribution is comparable to the present-day situation, with a group of samples plotting near the mantle array (*i.e.* $|\Delta\varepsilon_{Hf(t)}| < \sim 10$), a group with decoupled Hf and Nd isotopes ($\Delta\varepsilon_{Hf(t)}$ up to 97), and a few samples below the mantle array. The LREE-enriched (CO-015-B) and LREE-depleted (CO-084) harzburgites plot within the coupled and decoupled group, respectively.

6. Discussion

6.1. Re mobility and initial Os-isotope compositions

6.1.1. Post-magmatic disturbance of the Re—Os system

Cabo Ortegal pyroxenites are characterized by a wide range of $^{187}Os/^{188}Os$ (0.158–1.44) resulting from the ingrowth of radiogenic Os at highly variable $^{187}Re/^{188}Os$. Re contents range across 5 orders of magnitude (4 if excluding an outlier), but such values cannot have persisted for several hundred My, or present-day $^{187}Os/^{188}Os$ would be significantly higher. These observations indicate the mobility of Re and specify that it is mostly recent (Fig. 6). To tackle this issue, we used assimilation-fractional crystallization (AFC) models in which an average arc melt (Alves et al., 2002) interact with a high-Os assimilant represented by the highest-Os, best preferred sample from Cabo Ortegal (chromitite CO-080-B). Considering the uncertainties associated with the partition coefficients of Re and Os in complex mafic-ultramafic systems (*e.g.* Lorand and Luguet, 2016), we simply assumed that their relative partitioning varies across three orders of magnitude. These AFC models provide a first-order approximation of potential compositions for the peridotites, pyroxenites and chromitites after the main magmatic episode (Fig. 5). Conversely, samples outside this range have probably been affected by subsequent Re addition; Re/Os values exceeding ~10 for pyroxenites, and ~1 for chromitites are indeed unrealistic original compositions for such lithologies, although a wide range of Re/Os is commonly reported for pyroxenites (Carlson, 2005).

Neither Re concentrations nor $^{187}Re/^{188}Os$ correlate with the S contents in pyroxenites and peridotites, suggesting that Re addition is not directly related to the abundance of sulfides (Electronic Appendix 3 Fig. 1). However, high-$^{187}Re/^{188}Os$ samples have low Cu/S (*i.e.* <0.25) while samples with high Cu/S mostly have $^{187}Re/^{188}Os$ <15 (Fig. 10a and Electronic Appendix 3 Fig. 2). The range of Cu/S observed in the pyroxenites can be ascribed to the crystallization of Cu-rich sulfides (later exsolving chalcopyrite) during melt differentiation or to a metasomatic overprint during subsequent metamorphic evolution. Textural associations observed between interstitial chalcopyrite-rich sulfides and pre-kinematic amphibole suggest that they represent an intercumulus assemblage (Fig. 4b). Increasing Cu/S may thus relate to the co-precipitation of amphibole and sulfides from residual melts during the main magmatic episode. This is not directly reflected by the modal abundance of amphibole (Electronic Appendix 3 Fig. 4), because most amphibole in the pyroxenites is post-kinematic (*e.g.* Henry et al., 2017) and not associated with chalcopyrite-rich sulfides. Whether mineralogical or petrological factors have made Cu/S samples more sensitive to Re addition is unclear. However, Re addition seems to have preferentially affected samples in which little Cu addition (or conversely S loss) occurred to the system. A rough negative correlation exists between Mg# and $^{187}Re/^{188}Os$ (Electronic Appendix 3 Fig. 3) and distinct correlations are observed between $^{187}Re/^{188}Os$ and the modal abundance of amphibole in type-2 and -3 pyroxenites (Fig. 10b). Type-2 pyroxenites are also positively correlated with LREE enrichment (and Nd isotopes). Some extent of Re addition may have occurred during retrograde metamorphism, potentially due to the percolation of a hydrous fluids that resulted in the preferential amphibolitization of type-3, and to a lesser extent, of type-2 pyroxenites (Tilhac et al., 2016). However, type-1 pyroxenites have the lowest amphibole contents while they reach the highest $^{187}Re/^{188}Os$, suggesting that disturbance of the Re—Os system dominantly occurred during supergene alteration associated

Table 3
Lu and Hf abundances and Nd and Hf isotopic ratios of Cabo Ortegal pyroxenites and peridotites.

Sample		$^{147}Sm/^{144}Nd$	$^{143}Nd/^{144}Nd$	ε_{Nd}	Lu (ppm)	Hf (ppm)	$^{176}Lu/^{177}Hf$	$^{176}Hf/^{177}Hf$	2σ	ε_{Hf}	$\Delta\varepsilon_{Hf}$	$\Delta\varepsilon_{Hf(t)}$ at 390 Ma	Hf τ_{DM} (Ma)
Type-1 pyroxenites													
CO-091-A	Cpx	0.148	0.512662	0.6	0.05	0.05	0.139	0.283930	93	40	34	12	360
CO-094-B	Cpx	0.287	0.512965	6.5	0.05	0.07	0.097	0.283187	25	14	10	−3.3	−59
CO-095-A	Cpx	0.137	0.512598	−0.6	0.03	0.05	0.075	0.283199	8	15	10	2.5	−76
	Leached Cpx	0.137	0.512595	−0.7	0.03	0.05	0.075	0.283439	32	23	18	11	271
CO-096-B	Cpx	0.137	0.513103	9.2	0.03	0.03	0.113	0.283193	7	14	5.5	−7.3	−42
	Leached Cpx	0.137	0.513251	12	0.03	0.03	0.113	0.283464	43	24	11	2.3	153
	Amp	0.137	0.513221	12	0.21	0.17	0.170	0.283075	21	10	2.1	−26	−72
	WR	0.137	0.513271	12	0.03	0.07	0.063	0.283028	141	8.6	−4.6	−0.3	−487
Type-2 pyroxenites													
CO-006-A	Cpx	0.254	0.512837	4.0	0.02	0.04	0.078	0.283762	14	35	31	22	690
	Amp	0.296	0.512933	5.9	0.11	0.14	0.105	0.282167	148	−22	−25	−42	−879
CO-006-B	Cpx	0.143	0.512511	−2.3	0.01	0.11	0.008	0.284011	121	43	42	49	−1370
	WR	0.154	0.512666	0.7	0.05	0.20	0.035	0.284331	36	55	49	53	−23,000
CO-007	Cpx	0.285	0.512886	5.0	0.01	0.04	0.048	0.283823	67	37	35	32	3210
	Leached Cpx	0.285	0.512891	5.1	0.01	0.04	0.048	0.283018	24	8.2	5.9	3.3	−1370
CO-024	Cpx	0.167	0.512878	4.8	0.004	0.18	0.003	0.283192	37	14	3.1	21	91
	Leached Cpx	0.167	0.512937	6.0	0.004	0.18	0.003	0.283130	41	12	−0.9	19	186
	WR	0.178	0.512866	4.6	0.04	0.20	0.029	0.283245	168	16	6.3	16	35
CO-025	Cpx	0.086	0.512515	−2.2	0.03	0.07	0.060	0.282574	49	−7.5	−14	−16	−1670
	Leached Cpx	0.086	0.512609	−0.4	0.03	0.07	0.060	0.282986	56	7.1	−2.3	−1.1	−648
	WR	0.109	0.512595	−0.7	0.05	0.09	0.075	0.282184	206	−21	−28	−33	−1600
Type-3 pyroxenites													
CO-004-A	Cpx	0.106	0.512512	−2.3	0.03	0.14	0.036	0.283723	18	33	28	31	−10,300
	Amp	0.116	0.512545	−1.7	0.18	0.34	0.074	0.282936	37	5.3	0.3	−6.5	−472
	Amp*	0.116	0.512537	−1.8	0.18	0.34	0.074	0.283564	10	28	23	16	465
	WR	0.110	0.512523	−2.1	0.08	0.30	0.039	0.283624	66	30	25	27	26,600
CO-009	Cpx	0.098	0.512586	−0.9	0.02	0.05	0.056	0.285545	166	98	90	91	6490
	Leached Cpx	0.098	0.512580	−1.0	0.02	0.05	0.056	0.284062	46	45	38	38	2390
	Amp	0.077	0.512614	−0.3	0.16	0.35	0.061	0.285362	115	91	81	83	4740
	Leached Amp	0.077	0.512605	−0.5	0.16	0.35	0.061	0.283427	51	23	13	14	413
CO-010	Section 1	0.096	0.512520	−2.1	0.05	0.16	0.043	0.283435	21	23	17	19	2020
	Section 2	0.085	0.512494	−2.7	0.03	0.04	0.101	0.284000	19	43	37	24	637
	Section 3	0.149	0.512687	1.1	0.03	0.02	0.219	0.286930	225	147	140	97	1080
CO-067	Cpx	0.114	0.512552	−1.5	0.02	0.05	0.048	0.284210	22	50	45	45	5270
CO-101	Cpx	0.156	0.512613	−0.3	0.02	0.18	0.017	0.284104	91	47	43	50	−2150
Type-4 pyroxenites													
CO-002-A	Cpx	0.334	0.513000	7.2	0.03	0.03	0.159	0.283443	35	23	21	−11	85
CO-048	Cpx	0.071	0.512497	−2.6	0.02	0.05	0.073	0.283557	323	27	20	16	476
Harzburgites													
CO-015-B	WR	0.030	0.512401	−4.5	0.01	0.02	0.060	0.282952	57	5.9	−1.4	−2.1	−753
CO-084	WR	0.435	0.513294	13	0.03	0.06	0.068	0.284209	9	50	47	40	1700
Garnet-bearing mafic layer													
CO-026	WR	0.134	0.512522	−2.1	0.03	0.05	0.079	0.283240	8	16	13	3.1	−15

WR, whole rock; Cpx, clinopyroxene; Amp, amphibole. * coarse (> 600 μm) amphibole separates. Errors are given for the last digit on $^{176}Hf/^{177}Hf$. A decay constant of $\lambda_{Lu} = 1.865 \times 10^{-11}$ a^{-1} (Scherer et al., 2001) was used for age correction and model-age calculation. ε_{Hf} was calculated using present-day CHUR ratios of $^{176}Lu/^{177}Hf = 0.0336$ and $^{176}Hf/^{177}Hf = 0.282785$ (Bouvier et al., 2008) as $[(^{176}Hf/^{177}Hf_{sample})/(^{176}Hf/^{177}Hf_{CHUR}) - 1] \times 10{,}000$. Depleted mantle model ages were calculated using present-day DM ratios of $^{176}Lu/^{177}Hf = 0.0384$ and $^{176}Hf/^{177}Hf = 0.283251$ (Griffin et al., 2000). $\Delta\varepsilon_{Hf}$ was calculated using the Hf–Nd mantle array [$\varepsilon_{Hf} = (1.59\ \varepsilon_{Nd} + 1.28)$] of Chauvel et al. (2008). Sm–Nd isotope data from Tilhac et al. (2017).

with a late episode (*e.g.* serpentinization, crustal fluid circulation, weathering). This disturbance was potentially also responsible for vertical variations in platinum-group element (PGE) patterns reported in the Herbeira massif by Moreno et al. (2001), but this aspect is beyond the scope of this contribution..

6.1.2. Initial Os compositions, geochronology and tectonic implications

As discussed above, compositions representative of the original magmatic products are likely to be preserved in pyroxenite samples with low modal abundance of amphibole, high Mg# and high Cu/S (and/or high Cu). These samples indeed have the lowest $^{187}Re/^{188}Os$ and Re concentrations within the range of values obtained from the AFC models. All other pyroxenites have been excluded from this discussion as disturbance of the Re—Os system during metamorphism and/or late alteration could not be ruled out. Among the peridotites, strongly LREE-enriched sample CO-015-B has also been excluded. For the chromitites, in the absence of modal compositions and whole-rock S data, only the least serpentinized samples with Re concentrations within the range obtained from the AFC models ($^{187}Re/^{188}Os$ <3) were kept.

Preserved pyroxenites, peridotites and chromitites samples have relatively homogeneous $^{187}Os/^{188}Os$ (0.124–0.278), positively correlated to their $^{187}Re/^{188}Os$ (Fig. 11a). This correlation is unlikely to represent a mixing line, as suggested by the scattering observed on a $^{187}Os/^{188}Os$ *vs* 1/Os plot (Fig. 11b) although two weak trends might be identified. We show that age correction progressively brings these compositions along a single trend (Fig. 11b) and that significant radiogenic ingrowth (*i.e.* > ~600 Ma) would be required for these data to represent any reasonable mixing line. Instead, we believe that it constitutes an isochron with an age of 838 ± 42 Ma, probably dating the formation of Cabo Ortegal pyroxenites, acknowledging the fact that some initial isotopic heterogeneities (Fig. 11b) might add to the uncertainty of the isochron. This age, together with Nd model ages between 459 and 762 Ma (Tilhac et al., 2017), probably relates the main (Avalonian-Cadomian) magmatic activity of the arc documented by U—Pb and Hf-isotope systematics in zircon (Albert et al., 2015). It is also consistent with the metamorphic interpretation of U—Pb ages *ca* 500 Ma reported for the eclogite and granulite protoliths (*e.g.* Fernández-Suárez et al., 2007), unless the magmatic activity recorded by Cabo Ortegal pyroxenites was restricted to the mantle. Importantly, initial compositions obtained for the

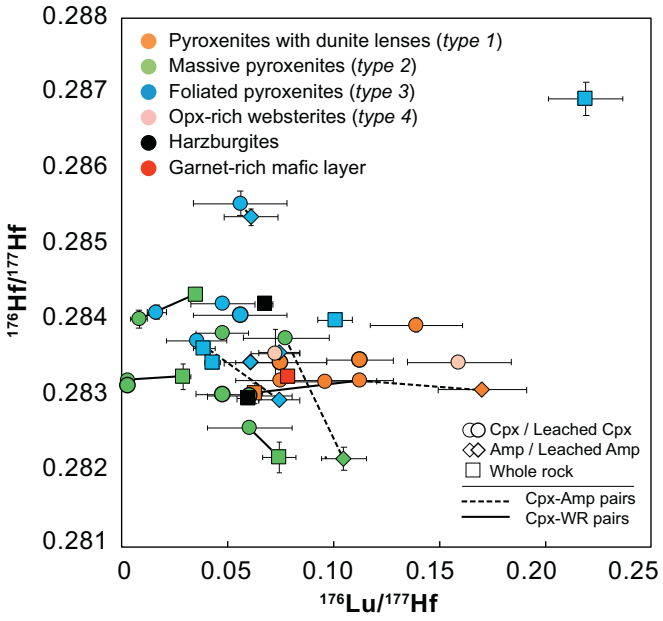

Fig. 7. $^{176}Hf/^{177}Hf$ *vs* $^{176}Lu/^{177}Hf$ of leached and unleached clinopyroxene (Cpx), amphibole (Amp) separates and whole-rock samples of Cabo Ortegal pyroxenites and peridotites. Error bars correspond to in-run errors for $^{176}Hf/^{177}Hf$ and whole-rock $^{176}Lu/^{177}Hf$, and to standard deviations (2σ) for the $^{176}Lu/^{177}Hf$ of the separates (Tilhac, 2017).

isochron and for the unradiogenic end members of the potential mixing discussed above are comparable ($^{187}Os/^{188}Os_{(i)} \sim 0.11$). These compositions correspond to $\tau_{RD(2)} = 2.3–2.8$ Ga, which overlap prominent peaks of zircon U—Pb ages at ~2.1 and ~2.7 Ga and interpreted as an evidence for the development of the arc on the northern margin of the Western African Craton (Albert et al., 2015). We suggest that the reworking of Paleoproterozoic to Archean material occurred during the main magmatic episode as the parental magmas of the pyroxenites intruded the marginal sub-continental lithospheric mantle (SCLM). Despite the relatively large error inherent in model-age calculations, our geochronological data are thus consistent with previous petrological, geochemical and geochronological constraints, and with regional geodynamics, indicating that Cabo Ortegal pyroxenites record the incipient stages of volcanic arc magmatism on an old continental margin (Tilhac et al., 2017, and references therein).

The initial compositions of Cabo Ortegal pyroxenites, peridotites and chromitites plot within the field defined by arc lavas (Fig. 12). Harzburgite CO-084 ($^{187}Os/^{188}Os_{(i)} = 0.114$) is comparable to other sub-arc mantle peridotites whose unradiogenic Os has been interpreted as a signature of ancient, melt-depleted residues (*e.g.* Parkinson et al., 1998), and is even less radiogenic than the depleted MORB mantle (Gannoun et al., 2007). The pyroxenites, and to a lesser extent, the chromitites have slightly higher $^{187}Os/^{188}Os_{(i)}$ comparable, for instance, to that of the most mafic lavas of the Lesser Antilles (0.127–0.20). While the latter have been interpreted as affected by various degrees of lower crustal assimilation (Bezard et al., 2015), this alternative is unlikely in the sub-arc mantle pyroxenites studied here. We thus believe that the relatively unradiogenic compositions preserved in Cabo Ortegal pyroxenites reflect the compositions of their parental arc melts, and hence of their source region. When compared to the range of radiogenic Os measured in arc lavas (Fig. 12), these results are consistent with limited slab contributions to the mantle wedge (Parkinson et al., 1998) and with the interpretation that radiogenic Os in erupted arc lavas mostly relates to the assimilation of crustal material (Bezard et al., 2015; Woodhead and Brauns, 2004). We emphasize that this observation remains valid regardless of the age-correction used (*i.e.* even present-day values are unradiogenic compared to arc lavas) and without bias towards high-Os samples.

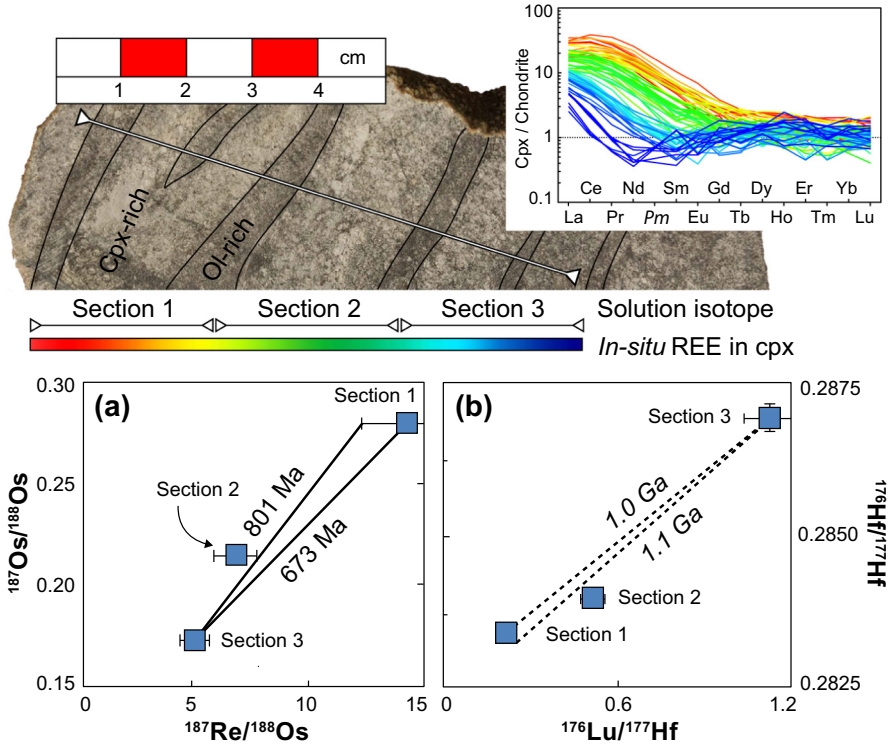

Fig. 8. (a) $^{187}Os/^{188}Os$ *vs* $^{187}Re/^{188}Os$ and (b) $^{176}Hf/^{177}Hf$ *vs* $^{176}Lu/^{177}Hf$ of composite sample CO-010 and corresponding Lu—Hf errorchron and Re—Os isochron. The location of the three sections analysed is shown with respect to the clinopyroxene REE profiles obtained by LA-ICP-MS (see text for further detail). Error bars correspond to in-run errors (2σ). Corresponding Sr- and Nd-isotope and REE compositions have been reported by Tilhac et al. (2017) and Tilhac et al. (2016), respectively.

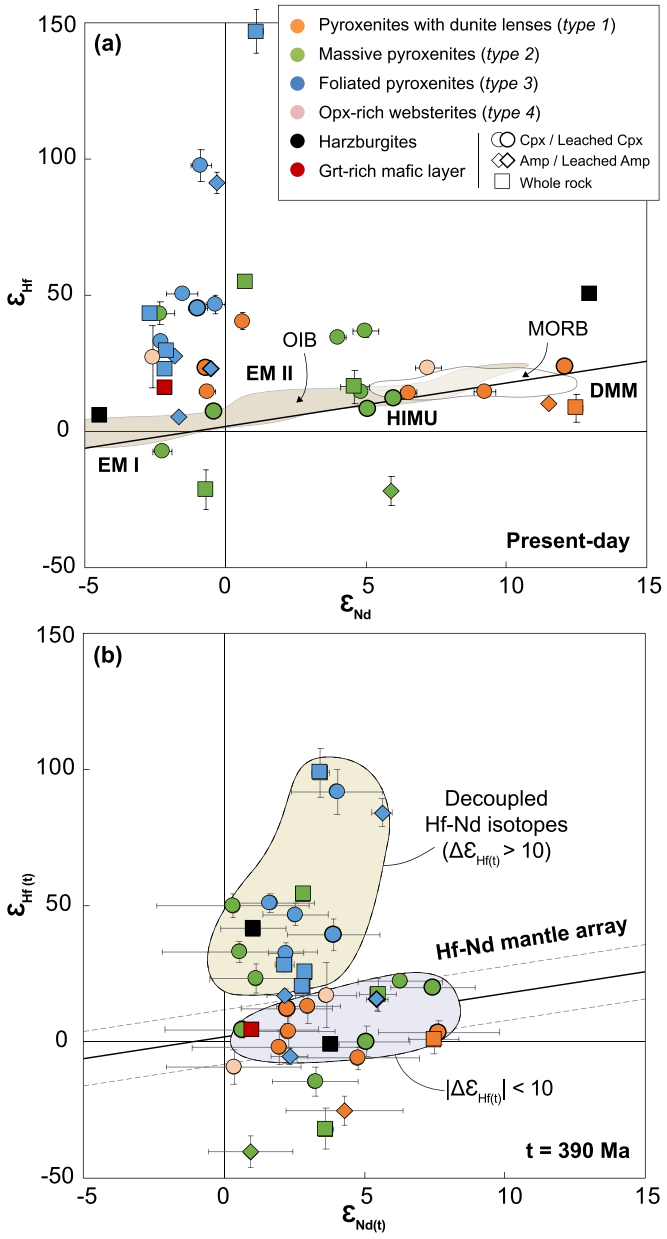

Fig. 9. Present-day (a) and age-corrected at $t = 390$ Ma (b) ε_{Hf} *vs* ε_{Nd} of leached and unleached clinopyroxene (Cpx) and amphibole (Amp) separates and whole-rock samples of Cabo Ortegal pyroxenites and peridotites. The compositional fields of MORB and OIB, and the Hf—Nd mantle array (± 10 ε_{Hf} units) of Chauvel et al. (2008) are shown for comparison. Nd-isotope compositions from Tilhac et al. (2017).

6.2. Lu—Hf constraints on melt-peridotite interaction and amphibolitization

Lu—Hf data collected on the Cabo Ortegal pyroxenites and peridotites are characterized by the absence of positive correlation between $^{176}Lu/^{177}Hf$ and $^{176}Hf/^{177}Hf$ (Fig. 7), and by the decoupling of the latter from Nd-isotope compositions (Fig. 9), especially in LREE-enriched samples. These results are significant despite the very low Hf concentrations (<0.20 ppm), because decoupling is consistently observed in the mineral separates, for which parent-daughter ratios were determined by LA-ICP-MS, and in whole-rock samples, for which solution ICP-MS was used. The absence of correlation between parent and daughter isotopes can be ascribed to either melt-peridotite interaction (*i.e.* forming pyroxenites that were initially isotopically heterogeneous) or subsequent disturbance of the system, for instance during retrograde metamorphism. Previous studies have provided geochemical (Tilhac et al., 2016), textural (Henry et al., 2017; Tilhac et al., 2016) and Sr- and Nd-isotope (Tilhac et al., 2017) evidence for a two-stage amphibolitization in Cabo Ortegal pyroxenites. According to this scenario, pre-kinematic amphibole crystallized from percolating and/or trapped residual melts, and post-kinematic crystals grew as a consequence of hydration (± addition of volatiles) of clinopyroxene and spinel during retrograde metamorphism. We examine below the impact of these processes on the Lu—Hf systematics.

6.2.1. Amphibolitization during hydrous retrograde metamorphism

Amphiboles separated from most type-2 and -3 (and to lesser extent from type-1) pyroxenites have lower $^{176}Hf/^{177}Hf$ despite having higher $^{176}Lu/^{177}Hf$ than the corresponding clinopyroxene. This disequilibrium cannot be solely explained by a metamorphic reaction *sensu stricto* as the difference in Lu/Hf due to clinopyroxene-amphibole partitioning would have led to more radiogenic Hf in amphibole. In sample CO-004-A, fine-grained (inclusion-free) amphibole has less radiogenic Hf than coexisting clinopyroxene while coarse-grained amphibole with abundant inclusions has $^{176}Hf/^{177}Hf$ within error of coexisting clinopyroxene, suggesting a contribution from these inclusions to the Hf budget. We note that in the few type-2 pyroxenites where garnet is preserved, clinopyroxene-orthopyroxene symplectites after garnet breakdown are observed including minor amphibole, ilmenite and Fe-Ti-rich spinel (Tilhac, 2017). Such symplectites are not common in Cabo Ortegal pyroxenites but they may have developed in samples where metamorphic garnet was present, most likely in evolved (high-Al_2O_3) type-2, and some type-3 pyroxenites. If the crystallization of metamorphic amphibole (now volumetrically dominant) occurred closely following the breakdown of garnet, it can be envisaged that some of these minor phases have remained as discrete inclusions in amphibole. Since ilmenite and Fe-Ti-rich spinel represent potential host minerals for HFSE (*e.g.* Pearson and Nowell, 2004), they could explain the disequilibrium between inclusion-free and inclusion-bearing amphibole, and the fact that this clinopyroxene-amphibole disequilibrium is mainly observed in evolved pyroxenites which most likely crystallized metamorphic garnet.

Retrograde metamorphism has been regionally estimated to have occurred at ~0.8 GPa and 500 °C in the ultramafic massifs of the Cabo Ortegal Complex (Ábalos et al., 2003). While it is reasonable to envisage that the post-kinematic amphibolitization of the peridotites and pyroxenites occurred under such conditions, it may also have been initiated during retrograde hydration under granulite-facies conditions, particularly if this episode was accompanied by the addition of volatile-rich fluids, for instance following the reaction: plagioclase + olivine + H_2O = clinopyroxene + amphibole + spinel + orthopyroxene. This reaction, documented in arc-related gabbroic lithologies (*e.g.* Greene et al., 2006), would be consistent with the isotopic disequilibrium between clinopyroxene and amphibole discussed above. The coexistence of plagioclase and amphibole is not directly documented in the pyroxenites, but the correlation between Eu/Eu* and Sr/Nd observed in type-2 pyroxenites (Tilhac et al., 2017) is consistent with this hypothesis. Type-2 pyroxenites plotting below the Hf—Nd mantle array could also be interpreted as metamorphosed, low-pressure (plagioclase-bearing) protoliths (Fig. 9b), although such lithologies could have been involved in their melt source, as suggested elsewhere (Montanini et al., 2012). Further investigation is required to specify the isotopic signature of the different amphibole generations, although their distinction in mineral concentrates is difficult. Nonetheless, considering the low solubility of Lu and Hf in sub-solidus hydrous fluids (Adam et al., 2014, and references therein), we consider it unlikely that the absence of correlation between $^{176}Lu/^{177}Hf$ and $^{176}Hf/^{177}Hf$ and the Hf—Nd isotopic decoupling relates to circulation of metamorphic fluids.

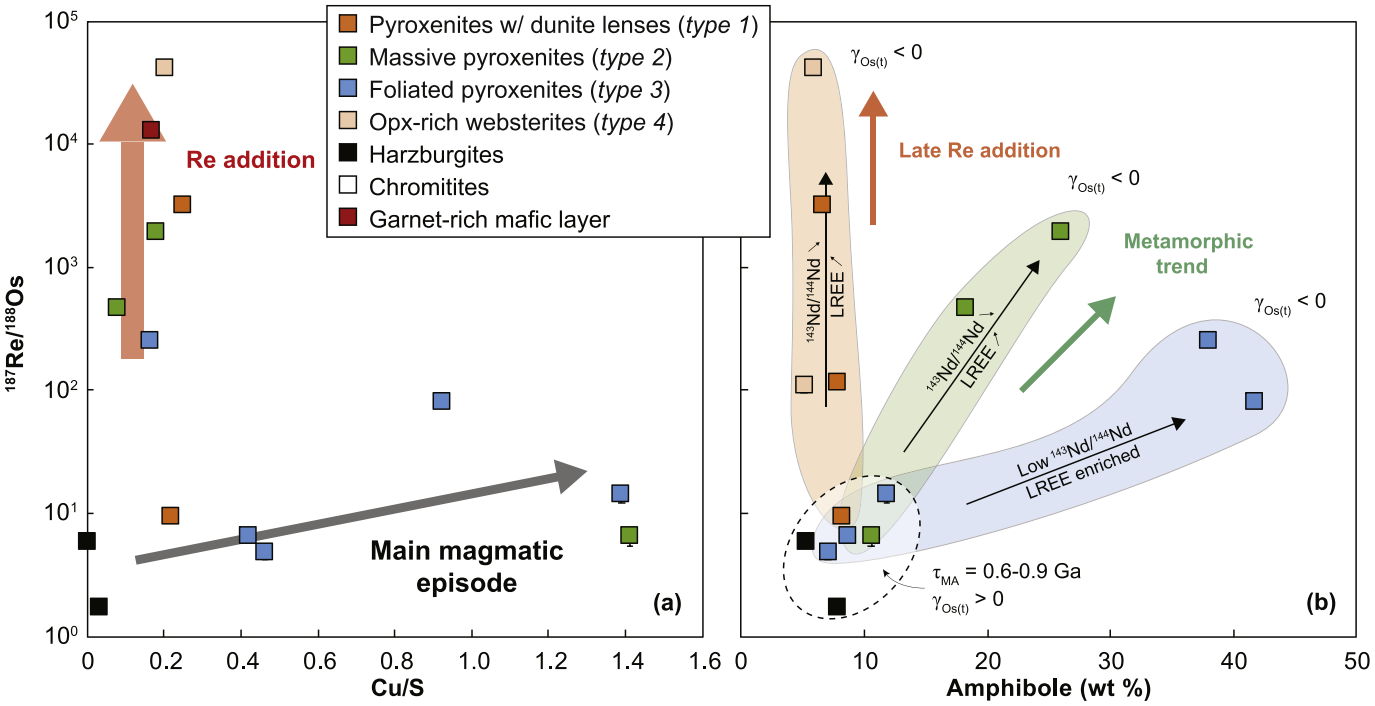

Fig. 10. $^{187}Re/^{188}Os$ (log scale) *vs* (a) Cu/S and (b) the modal abundance of amphibole in Cabo Ortegal pyroxenites and peridotites. Re addition is mostly independent to the increase in Cu/S and only partly related to metamorphic amphibolitization. $^{187}Re/^{188}Os$ positively correlates with amphibole content for type-2 and -3 pyroxenites, and with LREE (and Nd-isotope) enrichments for type-1, −2 and −4 pyroxenites. Only the least amphibolitized, low-$^{187}Re/^{188}Os$ samples have supra-chondritic age-corrected $^{187}Os/^{188}Os$ yielding Cambrian to Neoproterozoic τ_{MA}.

6.2.2. Melt-peridotite interaction

We now examine the potential development of chemical and/or isotopic disequilibrium during melt-peridotite interaction to account for the absence of parent-daughter correlation, and more specifically the slightly lower $^{176}Lu/^{177}Hf$ in type-2 pyroxenites with respect to type-1 pyroxenites (Fig. 7). The latter represent partial replacement products of peridotites, reflecting the percolation of a Si-undersaturated melt at decreasing melt/rock ratio (Tilhac et al., 2016). In contrast, type-2 pyroxenites are either the product of this melt-rock interaction at higher melt/rock ratios or crystal cumulates from Si-saturated melts (Fig. 3). Due to the relative partitioning of Lu and Hf between clinopyroxene and melt (most $Kd^{Lu/Hf}$ on the GERM database are >1.7 for basaltic melts; https://earthref.org), it is unlikely that Lu/Hf will decrease in clinopyroxene upon melt-peridotite interaction. For instance, assuming

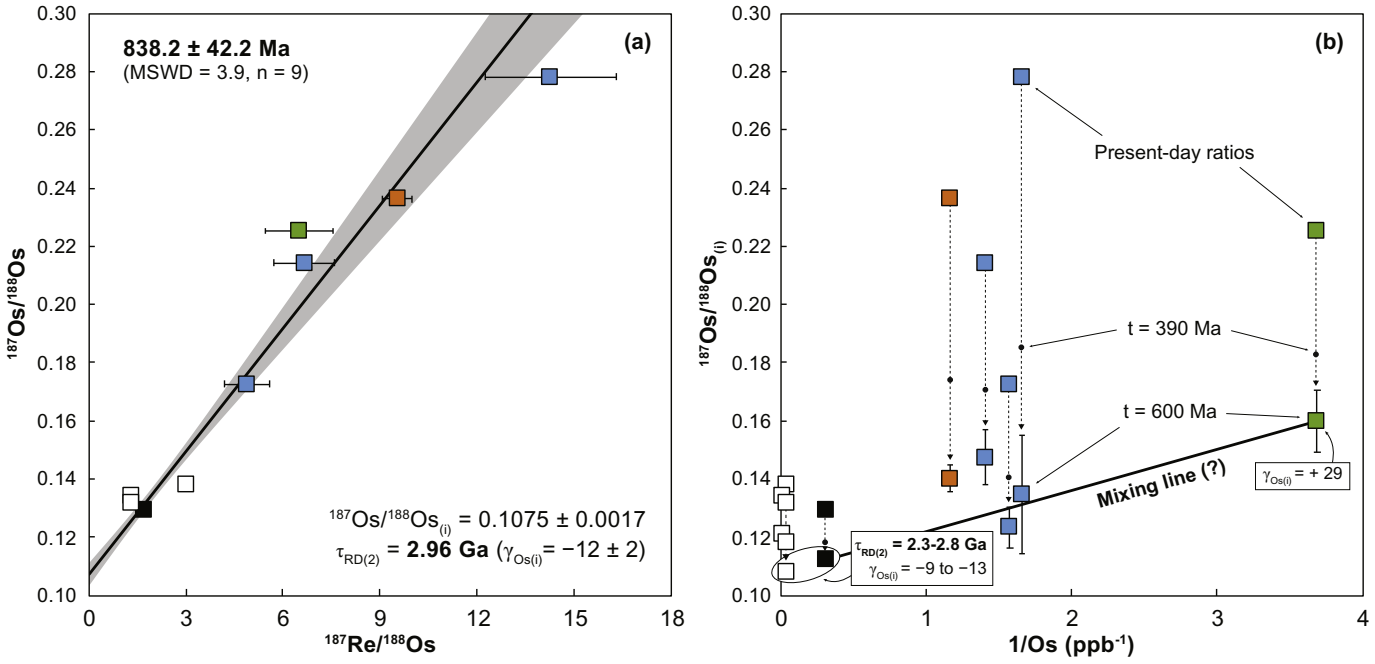

Fig. 11. (a) Re—Os isochron diagram showing the compositions of the preserved samples of pyroxenites, peridotites and chromitites; (b) $^{187}Os/^{188}Os_{(i)}$ *vs* 1/Os for the same set of samples showing the effect of age correction (from $t = 0$ to 600 Ma) on the collinearity of the data. A slight initial heterogeneity might have existed at > ~600 Ma bust the 1/Os plot mostly supports the reliability of the isochron age shown in (a). Other symbols as in Fig. 10.

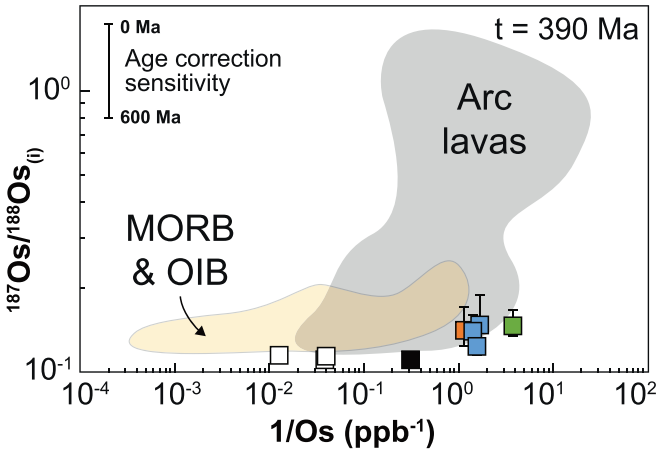

Fig. 12. $^{187}Os/^{188}Os_{(i)}$ *vs* 1/Os for the preserved samples of Cabo Ortegal pyroxenites, peridotites and chromitites, compared with the compositional fields of MORB, OIB, and arc lavas (Alves et al., 2002), corrected to the eruption age. The initial compositions (shown at t = 390 Ma) remain in the lower part of the arc field regardless of the age correction used, as shown by error bars corresponding to age correction up to 600 Ma. Both axes are in log scale. Other symbols as in Fig. 10.

$Kd^{Lu/Hf}_{clinopyroxene-melt} = 2.8$ (Table 4), a clinopyroxene typical of type-1 pyroxenites would maintain Lu/Hf ~ 1 (or even slightly increase) if it equilibrates with a melt with a Lu/Hf of 0.37, comparable to primitive picrites or boninites (*e.g.* Bénard et al., 2016). A significantly lower Lu/Hf is thus not expected in type-2 pyroxenites if they were solely the product of melt-rock reaction at higher melt/rock than type-1 pyroxenites. Instead, we believe that type-2 pyroxenites reflect the composition of a melt that has experienced some extent of fractional crystallization (Lu/Hf decreasing in the residual melts) and comparatively less melt-rock interaction than type-1 pyroxenites, whose relatively high Lu/Hf reflects the contribution of the host peridotites. Late partial melting of the type-1 pyroxenite protoliths is a possible alternative to this scenario, but no other evidence supports it. Our current Lu—Hf data, and in particular the lack of correlation between $^{176}Lu/^{177}Hf$ and $^{176}Hf/^{177}Hf$, are thus consistent with a combination of melt-peridotite interaction and fractional crystallization (Fig. 3), as proposed by Tilhac et al. (2016). We examine below the effect of such a melt-peridotite interaction for the decoupling of Hf and Nd isotopes; it could alternatively be envisaged that decoupling was acquired in the source region of the parental melts (*e.g.* Bizimis et al., 2005), but this is not consistent, among other, with the correlation of Hf model ages and $\Delta\varepsilon_{Hf}$ (Electronic Appendix 4 Fig. 1).

Table 4
Percolation-diffusion model parameters.

Percolation parameters			
Column length		500 m	
Melt velocity		5 cm/y	
Melt proportion (porosity)		1%/0.1%	
Modal composition		100% cpx	
Grain size		0.1 mm/1 mm	
Partition coefficients		Diffusivities	
		D_0 (m^2/s)	ε (kJ/mol)
Sm	0.293	$1.42.10^{-4}$	460.1
Nd	0.178	$5.54.10^{-4}$	483.9
Lu	0.449	Interpolated	
Hf	0.160	$4.81.10^{-4}$	233.1

Starting compositions	Peridotite (ppm)	Melt (ppm)
Sm	0.08	0.25
Nd	0.12	0.64
Lu	0.03	0.06
Hf	0.03	0.16
$^{147}Sm/^{144}Nd$	0.373	0.234
$^{176}Lu/^{177}Hf$	0.139	0.051
	at t = 390 Ma	*at t* = 390 Ma
$^{143}Nd/^{144}Nd_{(t)}$	0.513808	0.512216
$^{176}Hf/^{177}Hf_{(t)}$	0.285568	0.282791

Starting compositions were obtained as follows: for the peridotite, by 10% batch melting in the stability field of spinel (0.4 opx + 0.82 cpx + 0.08 spinel = melt +0.3 olivine; Chauvel and Blichert-Toft, 2001) at 2 Ga; for the melt, by mixing a DMM with 1% of a GLOSS eclogite batch melt (Tollstrup and Gill, 2005). For computation, isotopic ratios were converted into concentrations of individual isotopes (^{147}Sm, ^{143}Nd, ^{144}Nd, ^{176}Lu, ^{176}Hf and ^{177}Hf) based on their natural abundance (see Appendix A for more detail). Diffusivities are given as parameters of the Arrhenius relations $D = D_0\exp[(-\varepsilon + PV)/RT]$, with $V = 10^{-5}$ m^3/mol, $P = 1$ GPa and 1200 °C, for the REE (Van Orman et al., 2001), and $D = D_0 \exp.(-\varepsilon/RT)$, for Hf (Bloch and Ganguly, 2014); R is the gas constant. Partition coefficients from Chauvel and Blichert-Toft (2001).

6.3. Hf—Nd isotopic decoupling

Cabo Ortegal pyroxenites can be divided into a group of samples with coupled Hf and Nd isotopes and a group of samples displaying marked decoupling (Fig. 9). A few type-2 pyroxenite samples also plot below the mantle array, as discussed above, but these are not considered here. Generally, Hf—Nd isotopic decoupling can be reproduced, among other models, by mixing a component with radiogenic Hf and Nd and a component within the mantle array (*e.g.* Bizimis et al., 2003; Stracke et al., 2011). To be successful, such models require (1) the radiogenic component to be an ancient and/or highly depleted melting residue and (2) a mechanism to effectively re-equilibrate Nd isotopes prior to Hf and produce a concave-downward (effectively vertical) spread in Hf—Nd space. The former requirement can be reasonably met for Cabo Ortegal pyroxenites considering their Paleoproterozoic to Archean Os signature supported by zircon U—Pb ages (Albert et al., 2015). However, concave-downward Hf—Nd trends can be only obtained from a simple mixing (or an AFC) process if the radiogenic component has very high elemental Hf/Nd with respect to the unradiogenic component, which is not the case here. We are thus envisaging that Hf—Nd isotopic decoupling occurred during melt-peridotite interaction because of diffusional disequilibrium.

6.3.1. Melt-peridotite interaction (percolation-diffusion) models

Melt-peridotite interaction models have been previously used to simulate Hf—Nd isotopic decoupling (*e.g.* Stracke et al., 2011). In cases where relative elemental ratios between peridotite and melts are not sufficient, these models require a marked difference in Hf—Nd partitioning allowing Nd to be reset more readily than Hf (*i.e.* at lower melt/rock ratio). Although this condition may be met in many cases, we here focus on the role of diffusional reequilibration. For that purpose, we have simulated the percolation of an arc melt through a 2-Ga residual peridotite to explain the decoupling of Hf- and Nd-isotope compositions in Cabo Ortegal pyroxenites and peridotites (Table 4). The percolation-diffusion model used is based on a microstructural model for trace-element transfer (Oliveira et al., 2019) adapted for radiogenic isotope systems (Appendix A). Radioactive decay is negligible on the time scale of the percolation process, but it has been taken into account for consistency. Numerical simulations were run in a 500-m long, 1-D column with a solid composition assumed to be purely clinopyroxene (as it dominates the budget of Nd and Hf), a percolation rate of 5 cm/y comparable with previous porous-flow models (*e.g.* Keller and Katz, 2016) and various grain sizes and melt proportions (Table 4). Changes in modal proportions expected during such melt-peridotite interaction (*i.e.* increasing clinopyroxene content, changes in clinopyroxene/orthopyroxene ratios) have been ignored for simplicity; they have been studied elsewhere (Le Roux et al., 2009). Many starting compositions were possible, but we show that the model is mostly dependent on the percolation-diffusion parameters, as long as a sufficiently radiogenic component is involved.

The results show that a wide range of compositions can be obtained from the percolation-diffusion models while simple mixing between the same two components essentially gives a straight line on a $^{176}Hf/^{177}Hf$ *vs* $^{143}Nd/^{144}Nd$ plot (Fig. 13). To specifically illustrate the role of diffusional reequilibration, the same simulations were run using experimentally determined diffusivities (Fig. 13a) and assuming instantaneous reequilibration (infinitely fast diffusion; Fig. 13b) for elements and isotopes in the solid. Using infinite diffusivities, the bulk solid (and liquid) composition exhibits increasingly concave-upward Hf—Nd covariation trends from the bottom to the top of the column, as $Kd^{Hf} < Kd^{Nd}$ in the set of partition coefficients used (Chauvel and Blichert-Toft, 2001). These trends result from chemical fractionation processes predicted by the chromatographic model (Bodinier et al., 2004; Hauri, 1997; Navon and Stolper, 1987). Accordingly, their curvature is enhanced by low porosity (as shown in Fig. 13a for 0.1%) and impeded by large grain size (as shown for 1 mm). Compared with Cabo Ortegal pyroxenites, the compositions obtained with infinite diffusivities only overlap samples with non-decoupled Hf and Nd isotopes, but they fail to reproduce strong Hf—Nd decoupling above the mantle array. In contrast, using experimental diffusivities, solid compositions exhibit concave-downward covariation trends which overlap the compositions of most of Cabo Ortegal pyroxenites with decoupled Hf and Nd isotopes (Fig. 13b). In this case, the curvature decreases from the bottom to the top of the column because of the weak chromatographic effect that persists despite the slow diffusional re-equilibration. Using lower porosities increases the range of Hf—Nd compositions obtained across the column. For instance, the range obtained between 0 and 100 m for 0.1% melt exceeds the one obtained between 0 and 500 m for 1% melt (Fig. 13b). In the former case, solid compositions in the uppermost part of the column range from sinusoidal to concave-upward Hf—Nd covariation trends. Conversely, increasing the grain size results in less spatial differentiation and covariation trends obtained at different levels almost overlap (not shown).

Our percolation-diffusion models show that melt-peridotite interaction can effectively decouple Hf and Nd isotopes and that decoupling towards radiogenic Hf is enhanced by the strong diffusional disequilibrium that results from slow diffusional re-equilibration. These results particularly illustrate the competition between chromatographic effect and diffusional disequilibrium. On the one hand, low porosities and small grain sizes, which both enhance the chromatographic effect, tend to drive the Hf—Nd compositions towards the simple mixing line but slow diffusional re-equilibration impedes the process. On the other hand, diffusional disequilibrium creates varying chemical gradients between melt and peridotite as percolation proceeds in time and space (as can be noted from the dissymmetry of the covariation trends). In doing so, it produces isotopic decoupling towards radiogenic Hf even when the relative Kd values predict a chromatographic decoupling in the opposite direction. This is clearly shown if Fig. 13b as we deliberately used a set of partition coefficients with $Kd^{Hf} < Kd^{Nd}$ (Chauvel and Blichert-Toft, 2001).

No single combination of parameters is preferred to account for the isotopic heterogeneity of Cabo Ortegal pyroxenites, but the model results provide qualitative constraints. In particular, they point towards relatively large grain sizes (*e.g.* >100 μm) to create sufficient diffusional disequilibrium, (2) low porosities (*e.g.* <1%) to maintain some chromatographic effect and (3) temporal and/or spatial variability between the samples during the percolation process. Samples with coupled Hf and Nd isotopes (dominantly dunite-bearing, type-1 pyroxenites) were preferentially located at shallow magmatic levels (in the sense of a percolation column) and/or recorded melt-peridotite interaction at lower porosities. Note that, in this case, the model predicts that Hf-isotope compositions in the solid would be re-equilibrated with the percolating melt more readily than the Lu/Hf ratio (not shown), potentially accounting for the fact that samples with coupled Hf—Nd isotopes also have slightly higher Lu/Hf. These constraints are consistent with the petrogenetic scenario illustrated in Fig. 3a, although they imply a different geometry where type-1 pyroxenites would have rather developed

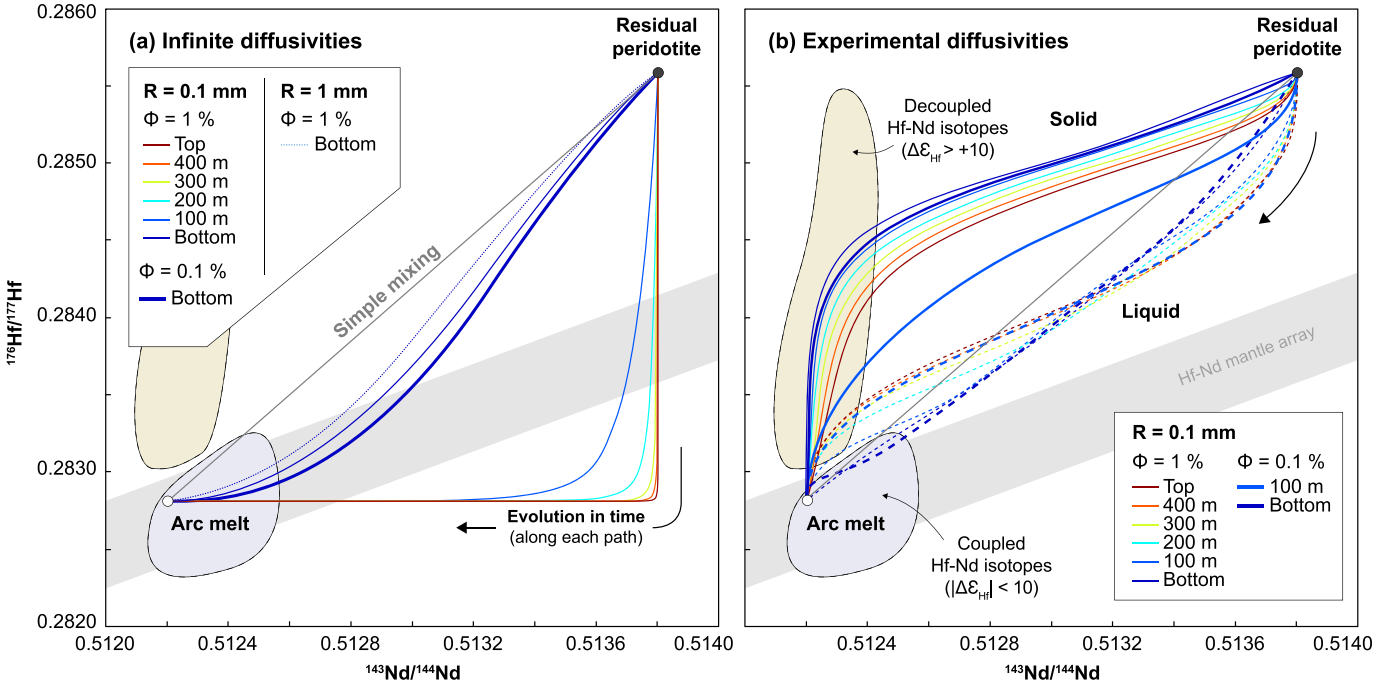

Fig. 13. $^{176}Hf/^{177}Hf$ *vs* $^{143}Nd/^{144}Nd$ obtained from the percolation-diffusion model using infinite (a) and experimentally determined diffusivities (b), compared with the two groups of Cabo Ortegal pyroxenites and peridotites with coupled and decoupled Hf—Nd isotopes. The modelled compositions of the solid (continuous lines) and liquid (dashed lines) evolve in space (as shown by the color of the different paths) and time (along each path), from the initial peridotite to final equilibrium with the melt. Starting compositions and the percolation-diffusion parameters are listed in Table 4; the model's governing equations and corresponding assumptions are presented in Appendix A. R, grain size; Φ, porosity (melt proportion). Note that Nd and Hf isotopes are age-corrected at 390 Ma for consistency but the actual melt-peridotite interaction process modelled occurred >600 Ma (*i.e.* main magmatic episode); the model results are essentially insensitive to the age correction.

at the termination of melt channels. Conversely, samples with strongly decoupled Hf and Nd isotopes probably required higher porosities. It is noteworthy that among these samples, many are foliated and highly amphibolitized (type-3). This is hard to reconcile with the fact that porosity-reducing reactions and grain-size reduction both enhance chromatography (Godard et al., 1995; Le Roux et al., 2009), unless the presence of amphibole had resulted in bulk $Kd^{Hf} > Kd^{Nd}$. This alternative is notably supported by the distribution of Hf and Nd between clinopyroxene and amphibole ($D^{Nd/Hf}_{amp-clinopyroxene} \ll 1$), especially in type-3 pyroxenites (< 0.2; Tilhac, 2017). Hf—Nd isotopic decoupling may have thus been favoured by the crystallization of amphibole during melt-peridotite interaction.

Despite the consistency of the constraints obtained from the model results, they are dependent on prescribed parameters that are worth special mention. These notably include the P-T-c dependencies of the diffusivities used, the rate of melt percolation (any faster rate would result in stronger disequilibrium) and the existence of other mineral phases and potential reactions between them and the percolating melt (with local changes in porosity). The inheritance of chemical and isotopic compositional variability, for instance due to initial depletion in the stability field of garnet (*e.g.* Schmidberger et al., 2002) or to the genesis of the parental melts in the presence of accessory minerals (Tollstrup and Gill, 2005) are also to be considered. A more complex, dynamically and thermodynamically constrained model is certainly possible (Oliveira et al., 2019), but the intent here is only to provide a conceptual framework for percolation-diffusion models of isotopic decoupling. This work followed on a previous work by Le Roux et al. (2009), who illustrated the role of the critical distance of isotopic homogenization (CDIH), *i.e.* the length characteristic to the rate at which isotopes re-equilibrate with respect to the percolation rate. A short CDIH (0.1–1 m) was notably suggested to account for Hf and Nd compositions of clinopyroxene separated from the Lherz peridotite, which is consistent with the use of experimental diffusivities in our percolation-diffusion models.

6.3.2. Implications for the preservation of ancient (reworked) SCLM domains

Comparison between diffusion-percolation models and the Hf and Nd isotopic variability of Cabo Ortegal pyroxenites suggests that melt-peridotite interaction between an arc magma and a 2-Ga residual peridotite is likely to result in strongly decoupled Hf and Nd isotopes. As discussed above, this decoupling may have been strengthen by earlier melt removal in the presence of garnet in the SCLM (Byerly and Lassiter, 2015) and the involvement of melts with particularly high Nd/Hf such as those commonly reported in arc magmas (*e.g.* Kelemen et al., 2014). The presence of SCLM-derived material and arc magmas in the Cabo Ortegal mantle is notably suggested by radiogenic Pb and EMI-like Sr- and Nd-isotope compositions (Santos et al., 2002) and compelling geological evidence (*e.g.* association of ophiolites and metamorphic mélanges, volcano-sedimentary protoliths, strong subduction signature, zircon provenance) discussed elsewhere (Albert et al., 2015; Martínez Catalán et al., 2009; Roper, 2016; Tilhac, 2017; Tilhac et al., 2016). On this basis, we suggest that the interaction of arc magmas and continental lithosphere may provide preferential conditions for Hf—Nd isotopic decoupling. Furthermore, mass-balance calculations suggest that up to 60% differentiation of primary basaltic arc basalts occurs *via* crystallization of high-Mg# pyroxenites (Müntener et al., 2001) but the latter represent only 5 to 35% of exposed arc crust (*e.g.* Greene et al., 2006). Primitive arc pyroxenites must form either within the igneous arc crust that extends below the seismic Moho (Kelemen et al., 2014) or be subsequently removed by delamination (Müntener et al., 2001). Although such processes are poorly quantified, notably because of the similar seismic velocities of peridotites and pyroxenites (Kelemen et al., 2014, and references therein), it is most likely that significant amounts of pyroxenite are introduced into the convective mantle during and/or following arc magmatism. We thus suggest that the ubiquitous recognition of Hf—Nd decoupling (*e.g.* Bizimis et al., 2003; Guarnieri et al., 2012; Pearson and Nowell, 2004; Salters and Zindler, 1995) reflects the presence of pyroxenite-rich (Hf-poor?) domains derived from ancient SCLM reworked by arc magmatism and recycled during subduction/collision cycles (O'Reilly et al., 2009). Although the Hf-isotope compositions of the cratonic mantle have been subject to debate (Byerly and Lassiter, 2015; Griffin et al., 2000; O'Reilly et al., 2009), this hypothesis would be consistent with the extensive preservation of reworked Archean SCLM, as suggested by the Global Lithospheric Architecture Mapping programme (GLAM; Begg et al., 2009).

7. Conclusions

We have examined the Lu—Hf and Re—Os isotope systematics and S concentrations in pyroxenites, peridotites and chromitites from the sub-arc mantle domain exposed in the Herbeira massif of the Cabo Ortegal Complex. The main findings are as follows:

(1) Disturbance of the Re—Os system most likely occurred during supergene alteration and preferentially affected low-Mg#, low Cu/S pyroxenites, although some Re addition may have occurred during hydrous retrograde metamorphism, as suggested by correlations between Re/Os, amphibole content and LREE enrichment.
(2) Samples protected from this disturbance display a clear correlation between $^{187}Re/^{188}Os$ and $^{187}Os/^{188}Os$ corresponding to an isochron age of 838 ± 42 Ma, which probably dates the formation of Cabo Ortegal pyroxenites; this is slightly older than the main Avalonian-Cadomian magmatic activity of the arc documented by Nd model ages and U—Pb zircon ages.
(3) Initial Os compositions are relatively unradiogenic, suggesting that very little slab-derived Os was transferred from the slab to the source region of the melts parental to the pyroxenites. These results are consistent with limited radiogenic-Os enrichment of the mantle wedge and with the interpretation that radiogenic Os in arc lavas mostly relates to the assimilation of crustal material.
(4) Paleoproterozoic to Archean model ages overlap prominent peaks of zircon U—Pb ages centred around ~2.1 and ~2.7 Ga, which are interpreted as evidence for the development of the arc next to the Western African Craton. Our data suggests that this ancient signature was acquired during that the intrusion of the pyroxenitic melts into subcontinental lithosphere, and that Cabo Ortegal pyroxenites record the incipient stages of the building of a volcanic arc on the continental margin.
(5) The absence of correlation between $^{176}Lu/^{177}Hf$ and $^{176}Hf/^{177}Hf$ and the Hf—Nd isotopic decoupling are mostly ascribed to melt-peridotite interaction, in good agreement with the results of our percolation-diffusion models. These numerical simulations notably show that Hf—Nd decoupling results from a trade-off between chromatographic effect and diffusional disequilibrium.
(6) Hf—Nd decoupling is enhanced by slow diffusional re-equilibration and can be relatively insensitive to chromatographic fractionation due to the relative partitioning of both elements, although in the case of Cabo Ortegal, Hf—Nd decoupling also may have been favoured by the crystallization of late-magmatic amphibole.
(7) It is suggested that arc-continent interaction provide preferential conditions for isotopic decoupling between Nd and Hf. As a corollary, the ubiquitous recognition of Hf—Nd decoupling in mantle peridotites and pyroxenites may reflect the contribution of recycled sub-arc mantle domains carrying the continental signature of ancient depletion events.

Acknowledgements

We would like to acknowledge N.J. Pearson for sharing his expertise and deep knowledge of geochemical analysis, P. Wieland for his analytical assistance and J. Girardeau for his support in the preparation of our fieldtrips. H. Henry is also thanked for our discussions during the preparation of this paper. This work was supported by the Australian Research Council grant for the ARC Centre of Excellence for Core to Crust Fluid Systems (CCFS), two Macquarie University International Postgraduate Scholarships (iMQRES), Macquarie postgraduate funds, and CNRS funds (UMR 5563, Géosciences Environnement Toulouse). The analytical data were obtained using instrumentation funded by DEST Systemic Infrastructure Grants, ARC LIEF, NCRIS/AuScope, industry partners and Macquarie University. This is contribution 1410 from the ARC Centre of Excellence for Core to Crust Fluid Systems (www.ccfs.mq.edu.au) and 1354 from the GEMOC Key Centre (www.gemoc.mq.edu.au) and is related to IGCP-662.

Declaration of Competing Interest

The authors declare that they have no known competing financial interests or personal relationships that could have appeared to influence the work reported in this paper.

Appendix A. Percolation-diffusion model

A.1. General approach

A numerical model is proposed to simulate the diffusion-controlled exchange of trace elements and the re-equilibration of their isotopic ratio during the percolation and reaction of a melt through a solid matrix. The formulation presented below takes into account both chemical and diffusional mass transfers, although in the particular setup used, it is assumed that no chemical reaction occurs between peridotite and melt (*i.e.* constant porosity).

The system is composed of solid mineral grains (*s*), approximated as spheres, and the percolating melt (*f*). The melt is assumed to reach equilibrium instantaneously with the minerals surface, which induces compositional gradients within the grains. This disequilibrium within the grains then tends to re-equilibrate with time by solid-state diffusion as the melt percolates through the solid matrix. Considering the lack of experimental constraints on the mathematical form following which isotopic ratios evolve during diffusion, the latter were converted into concentrations of individual isotopes based on their natural abundance. We assumed that these isotopes have the same partition coefficients and diffusivities than the corresponding elements; mass dependencies on these properties are thus considered negligible.

A.2. Model formulation

The concentration of a trace element *e*, and of its corresponding isotope *i* within a spherical grain of radii R_s is given by Fick's second law along the solid *s* characteristics (in spherical coordinates)

$$\begin{aligned}\frac{Dc^e}{Dt} &= D_s^e\left(\frac{\partial^2 c_s^e}{\partial r^2}+\frac{2}{r}\frac{\partial c_s^e}{\partial r}\right)\\ \frac{Dc^i}{Dt} &= D_s^i\left(\frac{\partial^2 c_s^i}{\partial r^2}+\frac{2}{r}\frac{\partial c_s^i}{\partial r}\right)\pm\lambda_i c_s^i\end{aligned} \tag{1}$$

where $c_s^{e,\,i}=c_s^{e,\,i}(r_s,t)$ is the concentration at a distance r_s from the center of the grain, $D_s^e=D_s^i$ is the diffusion coefficient for both the trace element *e* and its isotopes *i*, and λ_i is the decay constant (positive if i is a daughter isotope, or negative if it is a parent). Note that in order to accommodate phase changes in Eq. (1), the radii of the solid grains R_s may vary with time (*e.g.* $\frac{DR_s}{Dt}<0$ for partial melting).

Initial and boundary conditions of Eq. (1) are based on the assumption stated above of initial chemical equilibrium, instantaneous equilibration between melt and grain surfaces. In addition, radial symmetry is imposed on the compositional zoning within grains. These conditions read as follows

$$\begin{aligned}&\frac{c_{s,0}^{e,i}}{c_{f,0}^{e,i}}=K_s^{e,i}\\ &c_s^{e,i}\Big|_{r=R_s}=K_s^{e,i}c_f^{e,i}\\ &\frac{\partial c_s^{e,i}}{\partial r}\Big|_{r=0}=0\end{aligned} \tag{2}$$

where $K_s^{e,\,i}$ is the partition coefficient between mineral and melt, and $c_f^{e,\,i}$ is the concentration of the element *e*, or isotope *i*, in the melt.

The mass-balance equation for element *e*, or isotope *i*, in the melt is

$$\begin{aligned}&\frac{\partial\phi\rho_f c_f^e}{\partial t}+\nabla\cdot\left(\phi\rho_f c_f^e v_f\right)=\Gamma^e\\ &\frac{\partial\phi\rho_f c_f^i}{\partial t}+\nabla\cdot\left(\phi\rho_f c_f^i v_f\right)=\Gamma^i\pm\lambda_i\left(c_f^i+\Gamma^i\right)\end{aligned} \tag{3}$$

where ϕ is the porosity (*i.e.* melt proportion in volume), ρ is the density, v is the velocity, $\Gamma^{e,\,i}$ is the mass-transfer rate between solid grains and melt due to phase transformation (*i.e.* partial melting or crystallization) and diffusional re-equilibration within solid grains. A simple way to compute $\Gamma^{e,\,i}$ is to evaluate the gain/loss of a given element *e*, or isotope *i* within individual grains along their trajectories using the following integral

$$\Gamma^{e,i}=\frac{D_s}{Dt}\left[n_s\rho_s\int_0^{R_s(t)}4\pi r^2 c_s^{e,i}\,dr\right] \tag{4}$$

where $n_s=\frac{(1-\phi)}{4/3\pi R_s^3}$ refers to the number of grains per unit of volume (Iwamori, 1993; Oliveira et al., 2018). This formulation implicitly considers that the solid is monomineralic but its adaption to polymineralic assemblages is straightforward (Oliveira et al., 2019). Grain nucleation and coalescence are ignored in this formulation.

Eqs. (1)–(4) are solved numerically using a Eulerian-Lagrangian finite element method (Oliveira et al., 2016). At each time step, the concentrations in the solid grains (Eqs. (1)–(2)) and in the melt (Eqs. (3)–(4)) are computed iteratively until convergence is reached. An irregular mesh is used for the solid-grain diffusion problem (*e.g.* finer spatial discretization near the grain boundary).

Appendix B. Supplementary data

Supplementary data to this article can be found online at https://doi.org/10.1016/j.lithos.2019.105346.

References

Ábalos, B., Puelles, P., Gil Ibarguchi, J.I., 2003. Structural assemblage of high-pressure mantle and crustal rocks in a subduction channel (Cabo Ortegal, NW Spain). Tectonics 22, 1006–1027.

Ackerman, L., Bizimis, M., Haluzová, E., Sláma, J., Svojtka, M., Hirajima, T., Erban, V., 2016. Re–Os and Lu–Hf isotopic constraints on the formation and age of mantle pyroxenites from the Bohemian Massif. Lithos 256–257, 197–210.

Adam, J., Locmelis, M., Afonso, J.C., Rushmer, T., Fiorentini, M.L., 2014. The capacity of hydrous fluids to transport and fractionate incompatible elements and metals within the Earth's mantle. Geochem. Geophys. Geosyst. 15, 2241–2253.

Alard, O., Luguet, A., Pearson, N.J., Griffin, W.L., Lorand, J.-P., Gannoun, A., Burton, K.W., O'Reilly, S.Y., 2005. In situ Os isotopes in abyssal peridotites bridge the isotopic gap between MORBs and their source mantle. Nature 436, 1005–1008.

Albert, R., Arenas, R., Sánchez Martínez, S., Gerdes, A., 2012. The eclogite facies gneisses of the Cabo Ortegal complex (NW Iberian Massif): tectonothermal evolution and exhumation model. J. Iberian Geol. 38, 389–406.

Albert, R., Arenas, R., Gerdes, A., Sánchez Martínez, S., Fernández-Suárez, J., Fuenlabrada, J., 2015. Provenance of the variscan upper allochthon (cabo ortegal complex, NW Iberian Massif). Gondw. Res. 28, 1434–1448.

Alves, S., Schiano, P., Capmas, F., Allègre, C.J., 2002. Osmium isotope binary mixing arrays in arc volcanism. Earth Planet. Sci. Lett. 198, 355–369.

Arenas, R., Sánchez Martínez, S., Castiñeiras, P., Jeffries, T.E., Díez Fernández, R., Andonaegui, P., 2009. The basal tectonic mélange of the Cabo Ortegal complex (NW Iberian Massif): a key unit in the suture of Pangea. J. Iberian Geol. 35, 85–125.

Bedini, R.M., Blichert-Toft, J., Boyet, M., Albarède, F., 2004. Isotopic constraints on the cooling of the continental lithosphere. Earth Planet. Sci. Lett. 223, 99–111.

Begg, G.C., Griffin, W.L., Natapov, L.M., O'Reilly, S.Y., Grand, S.P., O'Neill, C.J., Hronsky, J.M.A., Djomani, Y.P., Swain, C.J., Deen, T., Bowden, P., 2009. The lithospheric architecture of Africa: Seismic tomography, mantle petrology, and tectonic evolution. Geosphere 5, 23–50.

Bénard, A., Nebel, O., Ionov, D.A., Arculus, R.J., Shimizu, N., Métrich, N., 2016. Primary Silica-rich Picrite and High-Ca Boninite Melt Inclusions in Pyroxenite Veins from the Kamchatka Sub-arc Mantle. J. Petrol. 57, 1955–1982.

Bezard, R., Schaefer, B.F., Turner, S., Davidson, J.P., Selby, D., 2015. Lower crustal assimilation in oceanic arcs: Insights from an osmium isotopic study of the Lesser Antilles. Geochim. Cosmochim. Acta 150, 330–344.

Bizimis, M., Sen, G., Salters, V.J.M., 2003. Hf–Nd isotope decoupling in the oceanic lithosphere: constraints from spinel peridotites from Oahu, Hawaii. Earth Planet. Sci. Lett. 217, 43–58.

Bizimis, M., Sen, G., Salters, V.J., Keshav, S., 2005. Hf-Nd-Sr isotope systematics of garnet pyroxenites from Salt Lake Crater, Oahu, Hawaii: evidence for a depleted component in Hawaiian volcanism. Geochim. Cosmochim. Acta 69, 2629–2646.

Blichert-Toft, J., Albarède, F., 1997. The Lu-Hf isotope geochemistry of chondrites and the evolution of the mantle-crust system. Earth Planet. Sci. Lett. 148, 243–258.

Bloch, E., Ganguly, J., 2014. 176Lu–176Hf and 147Sm–143Nd ages of the Martian shergottites: Evaluation of the shock-resetting hypothesis through diffusion kinetic experiments and modeling, and petrological observations. Earth Planet. Sci. Lett. 395, 173–183.

Bodinier, J.-L., Menzies, M.A., Shimizu, N., Frey, F.A., McPherson, E., 2004. Silicate, hydrous and carbonate metasomatism at Lherz, France: contemporaneous derivatives of silicate melt–harzburgite reaction. J. Petrol. 45, 299–320.

Bouvier, A., Vervoort, J.D., Patchett, P.J., 2008. The Lu–Hf and Sm–Nd isotopic composition of CHUR: Constraints from unequilibrated chondrites and implications for the bulk composition of terrestrial planets. Earth Planet. Sci. Lett. 273, 48–57.

Byerly, B.L., Lassiter, J.C., 2014. Isotopically ultradepleted domains in the convecting upper mantle: Implications for MORB petrogenesis. Geology. 42 (3), 203–206.

Byerly, B.L., Lassiter, J.C., 2015. Trace element partitioning and Lu–Hf isotope systematics in spinel peridotites from the Rio Grande Rift and Colorado Plateau: Towards improved age assessment of clinopyroxene Lu/Hf–176Hf/177Hf in SCLM peridotite. Chem. Geol. 413, 146–158.

Carlson, R.W., 2005. Application of the Pt–Re–Os isotopic systems to mantle geochemistry and geochronology. Lithos 82, 249–272.

Chauvel, C., Blichert-Toft, J., 2001. A hafnium isotope and trace element perspective on melting of the depleted mantle. Earth Planet. Sci. Lett. 190, 137–151.

Chauvel, C., Lewin, E., Carpentier, M., Arndt, N.T., Marini, J.-C., 2008. Role of recycled oceanic basalt and sediment in generating the Hf-Nd mantle array. Nat. Geosci. 1, 64–67.

Day, J.M.D., Waters, C.L., Schaefer, B.F., Walker, R.J., Turner, S., 2016. Use of Hydrofluoric Acid Desilicification in the Determination of Highly Siderophile Element Abundances and Re-Pt-Os Isotope Systematics in Mafic-Ultramafic Rocks. Geostand. Geoanal. Res. 40, 49–65.

Fernández-Suárez, J., Arenas, R., Abati, J., Martínez Catalán, J.R., Whitehouse, M.J., Jeffries, T.E., 2007. U-Pb chronometry of polymetamorphic high-pressure granulites: an example from the allochthonous terranes of the NW Iberian Variscan belt. Geol. Soc. Am. Mem. 200, 469–488.

Galán, G., Marcos, A., 1998. The high-pressure granulites of the Bacariza Formation: an earlier stage in the exhumation of other eclogites in the Cabo Ortegal complex (Hercynian belt, NW Spain). Trabajos de Geol. 141.

Gannoun, A., Burton, K.W., Parkinson, I.J., Alard, O., Schiano, P., Thomas, L.E., 2007. The scale and origin of the osmium isotope variations in mid-ocean ridge basalts. Earth Planet. Sci. Lett. 259, 541–556.

Garrido, C.J., Bodinier, J.-L., 1999. Diversity of mafic rocks in the Ronda peridotite: evidence for pervasive melt–rock reaction during heating of subcontinental lithosphere by upwelling asthenosphere. J. Petrol. 40, 729–754.

Gil Ibarguchi, J.I., Ábalos, B., Azcarraga, J., Puelles, P., 1999. Deformation, high-pressure metamorphism and exhumation of ultramafic rocks in a deep subduction/collision setting (Cabo Ortegal, NW Spain). J. Metam. Geol. 17, 747–764.

Girardeau, J., Gil Ibarguchi, J.I., 1991. Pyroxenite-rich peridotites of the Cabo Ortegal complex (Northwestern Spain): evidence for large-scale upper-mantle heterogeneity. J. Petrol. Spec. Lherzolites Issue 135–154.

Girardeau, J., Gil Ibarguchi, J.I., Ben Jamaa, N., 1989. Evidence for a Heterogeneous Upper Mantle in the Cabo Ortegal complex, Spain. Science 245, 1231–1233.

Godard, M., Bodinier, J.-L., Vasseur, G., 1995. Effects of mineralogical reactions on trace element redistributions in mantle rocks during percolation processes: a chromatographic approach. Earth Planet. Sci. Lett. 133, 449–461.

Greene, A.R., DeBari, S.M., Kelemen, P.B., Blusztajn, J., Clift, P.D., 2006. A detailed geochemical study of Island Arc crust: the Talkeetna Arc Section, South–Central Alaska. J. Petrol. 47, 1051–1093.

Griffin, W.L., Pearson, N.J., Belousova, E., Jackson, S.E., van Achterbergh, E., O'Reilly, S.Y., Shee, S.R., 2000. The Hf isotope composition of cratonic mantle: LAM-MC-ICPMS analysis of zircon megacrysts in kimberlites. Geochim. Cosmochim. Acta 64, 133–147.

Guarnieri, L., Nakamura, E., Piccardo, G.B., Sakaguchi, C., Shimizu, N., Vannucci, R., Zanetti, A., 2012. Petrology, trace element and Sr, Nd, Hf isotope geochemistry of the North Lanzo Peridotite Massif (Western Alps, Italy). J. Petrol. 53, 2259–2306.

Hauri, E.H., 1997. Melt migration and mantle chromatography, 1: simplified theory and conditions for chemical and isotopic decoupling. Earth Planet. Sci. Lett. 153, 1–19.

Henry, H., Tilhac, R., Griffin, W.L., O'Reilly, S.Y., Satsukawa, T., Kaczmarek, M.-A., Grégoire, M., Ceuleneer, G., 2017. Deformation of mantle pyroxenites provides clues to geodynamic processes in subduction zones: a case study of the Cabo Ortegal complex, Spain. Earth Planet. Sci. Lett. 472, 174–185.

Huong, L., Otter, L., Förster, M., Hauzenberger, C., Krenn, K., Alard, O., Macholdt, D., Weis, U., Stoll, B., Jochum, K., 2018. Femtosecond laser ablation-ICP-mass spectrometry and CHNS elemental analyzer reveal trace element characteristics of danburite from Mexico, Tanzania, and Vietnam. Minerals 8.

Ionov, D.A., Blichert-Toft, J., Weis, D., 2005. Hf isotope compositions and HREE variations in off-craton garnet and spinel peridotite xenoliths from Central Asia. Geochim. Cosmochim. Acta 69, 2399–2418.

Iwamori, H., 1993. Dynamic disequilibrium melting model with porous flow and diffusion-controlled chemical equilibration. Earth Planet. Sci. Lett. 114, 301–313.

Jweda, J., Bolge, L., Class, C., Goldstein, S.L., 2016. High Precision Sr-Nd-Hf-Pb Isotopic Compositions of USGS Reference Material BCR-2. Geostand. Geoanal. Res. 40, 101–115.

Kelemen, P.B., Hanghøj, K., Greene, A.R., 2014. One view of the geochemistry of subduction-related magmatic arcs, with an emphasis on primitive andesite and lower crust. In: Turekian, K.K. (Ed.), Treatise on Geochemistry, Second edition Elsevier, Oxford, pp. 749–806.

Keller, T., Katz, R.F., 2016. The role of volatiles in reactive melt transport in the asthenosphere. J. Petrol. 57, 1073–1108.

Lambart, S., Baker, M.B., Stolper, E.M., 2016. The role of pyroxenite in basalt genesis: Melt-PX, a melting parameterization for mantle pyroxenites between 0.9 and 5 GPa. J. Geophys. Res. Solid Earth 121, 5708–5735.

Le Roux, V., Bodinier, J.L., Alard, O., O'Reilly, S.Y., Griffin, W.L., 2009. Isotopic decoupling during porous melt flow: a case-study in the Lherz peridotite. Earth Planet. Sci. Lett. 279, 76–85.

Lorand, J.-P., 1991. Sulphide petrology and sulphur geochemistry of orogenic Lherzolites: a comparative study of the pyrenean bodies (France) and the Lanzo Massif (Italy). J. Petrol. Special_Volume, 77–95.

Lorand, J.-P., Luguet, A., 2016. Chalcophile and siderophile elements in mantle rocks: Trace elements controlled by trace minerals. Rev. Mineral. Geochem. 81, 441–488.

Lu, J., Griffin, W.L., Tilhac, R., Xiong, Q., Zheng, J., O'Reilly, S.Y., 2018. Tracking deep lithospheric events with Garnet-Websterite Xenoliths from Southeastern Australia. J. Petrol. 59, 901–930.

Martínez Catalán, J.R., Arenas, R., Abati, J., Sánchez Martínez, S., Díaz García, F., Fernández Suárez, J., González Cuadra, P., Castiñeiras, P., Gómez Barreiro, J., Díez Montes, A., 2009. A rootless suture and the loss of the roots of a mountain chain: the Variscan belt of NW Iberia. Comp. Rend. Géosci. 341, 114–126.

Montanini, A., Tribuzio, R., 2015. Evolution of recycled crust within the mantle: Constraints from the garnet pyroxenites of the External Ligurian ophiolites (northern Apennines, Italy). Geology. 43 (10), 911–914.

Montanini, A., Tribuzio, R., Thirlwall, M., 2012. Garnet clinopyroxenite layers from the mantle sequences of the Northern Apennine ophiolites (Italy): evidence for recycling of crustal material. Earth Planet. Sci. Lett. 351–352, 171–181.

Moreno, T., Gibbons, W., Prichard, H.M., Lunar, R., 2001. Platiniferous chromitite and the tectonic setting of ultramafic rocks in Cabo Ortegal, NW Spain. J. Geol. Soc. Lond. 158, 601–614.

Müntener, O., Kelemen, P.B., Grove, T.L., 2001. The role of H_2O during crystallization of primitive arc magmas under uppermost mantle conditions and genesis of igneous pyroxenites: an experimental study. Contrib. Mineral. Petrol. 141, 643–658.

Navon, O., Stolper, E., 1987. Geochemical consequences of melt percolation: the upper mantle as a chromatographic column. J. Geol. 285–307.

Oliveira, B., Afonso, J.C., Zlotnik, S., 2016. A Lagrangian–Eulerian finite element algorithm for advection–diffusion–reaction problems with phase change. Comput. Methods Appl. Mech. Eng. 300, 375–401.

Oliveira, B., Afonso, J.C., Zlotnik, S., Diez, P., 2018. Numerical modelling of multiphase multicomponent reactive transport in the Earth's interior. Geophys. J. Int. 212, 345–388.

Oliveira, B., Tilhac, R., Afonso, J.C., 2019. Multi-phase multi-component reactive transport: towards a unified modelling approach to mantle magmatism. J. Petrol. (Submitted).

Ordóñez Casado, B., Gebauer, D., Schäfer, H.J., Gil Ibarguchi, J.I., Peucat, J.-J., 2001. A single devonian subduction event for the HP/HT metamorphism of the Cabo Ortegal complex within the Iberian Massif. Tectonophysics 332, 359–385.

O'Reilly, S.Y., Zhang, M., Griffin, W.L., Begg, G., Hronsky, J., 2009. Ultradeep continental roots and their oceanic remnants: a solution to the geochemical "mantle reservoir" problem? Lithos 112, 1043–1054.

Parkinson, I.J., Hawkesworth, C.J., Cohen, A.S., 1998. Ancient mantle in a modern arc: Osmium isotopes in Izu-Bonin-Mariana forearc peridotites. Science 281, 2011–2013.

Patchett, P.J., Tatsumoto, M., 1980. Hafnium isotope variations in oceanic basalts. Geophys. Res. Lett. 7, 1077–1080.

Pearson, D.G., Nowell, G.M., 2004. Re–Os and Lu–Hf isotope constraints on the origin and age of pyroxenites from the Beni Bousera Peridotite Massif: implications for mixed Peridotite–Pyroxenite Mantle sources. J. Petrol. 45, 439–455.

Puelles, P., Gil Ibarguchi, J.I., Beranoaguirre, A., Ábalos, B., 2012. Mantle wedge deformation recorded by high-temperature peridotite fabric superposition and hydrous retrogression (Limo massif, Cabo Ortegal, NW Spain). Int. J. Earth Sci. 101, 1835–1853.

Roper, R.A., 2016. The Eclogitic Gneisses of the Cabo Ortegal Complex: Provenance and Tectonothermal Evolution (Zircon U-Pb/Lu-Hf Methods).

Salters, V.J.M., Zindler, A., 1995. Extreme 176Hf/177Hf in the sub-oceanic mantle. Earth Planet. Sci. Lett. 129, 13–30.

Salters, V.J.M., Mallick, S., Hart, S.R., Langmuir, C.E., Stracke, A., 2011. Domains of depleted mantle: new evidence from hafnium and neodymium isotopes. Geochem. Geophys. Geosyst. 12 (n/a-n/a).
Sanfilippo, A., Salters, V., Tribuzio, R., Zanetti, A., 2019. Role of ancient, ultra-depleted mantle in Mid-Ocean-Ridge magmatism. Earth Planet. Sci. Lett. 511, 89–98.
Santos, J.F., Schärer, U., Gil Ibarguchi, J.I., Girardeau, J., 2002. Genesis of pyroxenite-rich peridotite at Cabo Ortegal (NW Spain): geochemical and Pb–Sr–Nd isotope data. J. Petrol. 43, 17–43.
Scherer, E., Münker, C., Mezger, K., 2001. Calibration of the lutetium-hafnium clock. Science 293, 683–687.
Schmidberger, S.S., Simonetti, A., Francis, D., Gariépy, C., 2002. Probing Archean lithosphere using the Lu–Hf isotope systematics of peridotite xenoliths from Somerset Island kimberlites, Canada. Earth Planet. Sci. Lett. 197, 245–259.
Sorbadere, F., Médard, E., Laporte, D., Schiano, P., 2013. Experimental melting of hydrous peridotite–pyroxenite mixed sources: constraints on the genesis of silica-undersaturated magmas beneath volcanic arcs. Earth Planet. Sci. Lett. 384, 42–56.
Stracke, A., Snow, J.E., Hellebrand, E., von der Handt, A., Bourdon, B., Birbaum, K., Günther, D., 2011. Abyssal peridotite Hf isotopes identify extreme mantle depletion. Earth Planet. Sci. Lett. 308, 359–368.
Tilhac, R., 2017. Petrology and geochemistry of pyroxenites from the Cabo Ortegal complex, Spain. Macquarie Univ. 230.
Tilhac, R., Ceuleneer, G., Griffin, W.L., O'Reilly, S.Y., Pearson, N.J., Benoit, M., Henry, H., Girardeau, J., Grégoire, M., 2016. Primitive arc magmatism and delamination: petrology and geochemistry of pyroxenites from the Cabo Ortegal complex, Spain. J. Petrol. 57, 1921–1954.
Tilhac, R., Grégoire, M., O'Reilly, S.Y., Griffin, W.L., Henry, H., Ceuleneer, G., 2017. Sources and timing of pyroxenite formation in the sub-arc mantle: Case study of the Cabo Ortegal complex, Spain. Earth Planet. Sci. Lett. 474, 490–502.
Tollstrup, D.L., Gill, J.B., 2005. Hafnium systematics of the Mariana arc: evidence for sediment melt and residual phases. Geology 33.
Van Orman, J.A., Grove, T.L., Shimizu, N., 2001. Rare earth element diffusion in diopside: influence of temperature, pressure, and ionic radius, and an elastic model for diffusion in silicates. Contrib. Mineral. Petrol. 141, 687–703.
Walker, R., Morgan, J., 1989. Rhenium-osmium isotope systematics of carbonaceous chondrites. Science 243, 519–522.
Widom, E., 2011. Recognizing recycled osmium. Geology 39, 1087–1088.
Woodhead, J., Brauns, M., 2004. Current limitations to the understanding of Re–Os behaviour in subduction systems, with an example from New Britain. Earth Planet. Sci. Lett. 221, 309–323.